Connectional architecture of the prefrontal cortex in the marmoset brain

Akiya Watakabe[1*], Henrik Skibbe[2*], Ken Nakae[3], Hiroshi Abe[1], Noritaka Ichinohe[1,4], Jian Wang[1], Masafumi Takaji[1], Hiroaki Mizukami[5], Alexander Woodward[6], Rui Gong[6], Junichi Hata[7,8], Hideyuki Okano[7,9], Shin Ishii[3], Tetsuo Yamamori[1*]

Author affiliations

[1]Laboratory for Molecular Analysis of Higher Brain Function, RIKEN Center for Brain Science, 2-1 Hirosawa, Wako, Saitama, Japan.

[2]Brain Image Analysis Unit, RIKEN Center for Brain Science, 2-1 Hirosawa, Wako, Saitama, Japan.

[3]Integrated Systems Biology Laboratory, Department of Systems Science, Graduate School of Informatics, Kyoto University, 36-1 Yoshida-Honmachi, Sakyo, Kyoto, Japan.

[4]Department of Ultrastructural Research, National Institute of Neuroscience, National Center of Neurology and Psychiatry, Kodaira, Tokyo, Japan

[5]Division of Genetic Therapeutics, Center for Molecular Medicine, Jichi Medical University, Shimotsuke, Tochigi, Japan.

[6]Connectome Analysis Unit, RIKEN Center for Brain Science, 2-1 Hirosawa, Wako, Saitama, Japan.

[7]Laboratory for Marmoset Neural Architecture, RIKEN Center for Brain Science, 2-1 Hirosawa, Wako, Saitama, Japan.

[8]Graduate School of Human Health Sciences, Tokyo Metropolitan University, Arakawa, Tokyo, Japan

[9]Department of Physiology, Keio University School of Medicine, Tokyo, Japan.

Corresponding authors[*]

Akiya Watakabe, akiya.watakabe@riken.jp, Henrik Skibbe, henrik.skibbe@riken.jp, Tetsuo Yamamori, tetsuo.yamamori@riken.jp

Abstract

The primate prefrontal cortex (PFC) has greatly expanded to evolve specialized architecture, but its roles in top-down brain control remain enigmatic. Based on connectomics mapping of the marmoset PFC, we characterized two contrasting features of corticocortical and corticostriatal projections. One is the 'focalness' of projections, exemplified by multiple columnar axonal terminations in the cortical layers and the other is the 'widespreadness' of weaker projections, whose patterns consisted of several common motifs representing the framework of PFC connectivity. We clarified the topographic rules of distribution for these features, which should constrain how PFC neurons can coordinate to control the target regions as populations. These features are observed only primitively in rodents and are considered critical in understanding the roles of the PFC in neuropsychiatric disorders.

Introduction

The prefrontal cortex (PFC) plays a central role in orchestrating the activities of various brain regions to achieve complex behaviors involving cognitive and emotional functions, and its malfunction leads to mental disorders(*1*, *2*). Its expansion and specialization are conspicuous traits of the primate lineage, including humans. Since the PFC is simultaneously connected to various cortical and subcortical regions(*1–3*), detailed information at the whole-brain scale is necessary to fully understand its top-down influences on other brain regions. Recent advancements in imaging and computation techniques realized high-throughput retrieval and analysis of a large amount of neuronal tracing data for the whole mouse brain(*4–6*). Considering the effectiveness of such a big data approach, the application of a similar whole-brain strategy to primates is desired.

The common marmoset has recently been favored as a non-human primate model for neuroscience studies(*7*, *8*). The marmoset cortex is significantly smaller and simpler than that of macaques, but its overall architecture retains clear signs of primate traits, including the existence of frontal eye field (FEF) and area V5 (MT), whose homologs are not clear in rodents(*8*). Its PFC consists of similar subregions as those of macaques, including the granular PFC, which is missing in rodents(*1*, *7*). Furthermore,

an increasing number of studies have used marmosets for detailed structural and functional MRI studies(*9–12*), which should aid comparison with macaques and humans. To gain better knowledge on PFC connectivity in primates, here we performed whole-brain anterograde axonal tracing of common marmosets. In this paper, we focused on corticocortical and corticostriatal projections of the PFC with two unresolved issues in mind. One was the characterization of mesoscale structures, represented by the 'columnar' axonal convergence of the submillimeter scale(*13–15*). Such structures have been known for decades but not systematically characterized to date. The other was the characterization of weak and sparse projections, whose significance came to be noticed with the development of more sensitive tracers(*6*, *16*, *17*).

Results

Serial two-photon tomography imaging in the marmoset brain

The key of our project was the implementation of serial two-photon tomography(*4*) for the marmoset brain. Combined with the highly bright Tet-enhanced AAV vector system, our experimental setup met two requirements that were critical for our purposes: sensitive detection of the axonal signals and accurate reconstruction of the 3D volume. The high quality of our volume imaging was best exemplified by the reconstruction of columnar axonal spread in the cortex (Fig. 1A and Supplementary Movies 1 and 2). Our data also allowed smooth conversion of the bent cortical layers into a stack of flatmaps ('flatmap stack') (Fig. S1A-C), in which tangentially focal signals appeared as many discrete spots or foci (e.g., the white arrows in Fig. 1A-C. See also Fig. S1E). In the raw section image data, these focal projections comprised dense axonal branches, whereas the adjacent region only had sparse axonal signals (Fig. 1C, right panels, compare 'in' and 'out', Fig. S1D). Our imaging also revealed the 'widespreadness' of weak and sparse signals. Fig. 1D and 1E show the same data used for Fig. 1A and 1B, but at a significantly lower threshold and with log-transformation. The abundant weaker projections toward the parietal areas (Fig. 1E, par) and sparse parahippocampal projections were detected (Fig. 1E, cyan arrow; see Fig. S1F for original section view). Thus, the 'focalness' and 'widespreadness' of PFC projections were reproduced in the standardized forms for quantitative evaluation.

The current study aimed to explore how these two types of projections originate from different subregions of the PFC. This study placed 44 injections into six

subregions of the PFC (frontopolar cortex [FP], dorsolateral PFC_dorsal [dlPFCd], dorsolateral PFC_ventral [dlPFCv], dorsomedial PFC [dmPFC], anterior cingulate cortex [ACC], orbitofrontal cortex [OFC]), as well as into ventrolateral PFC (vlPFC), and caudally positioned premotor and dorsal ACC areas (PM and dACC) (Fig. 1F, Fig. S1J and Table S1, also see Fig. S2). As shown in Fig. 1G and Fig. S1K, the simple overlay of projections from these subregions showed two conspicuous features of PFC projections. First, PFC projections skipped the primary motor, somatosensory, and auditory areas and innervated the association areas in the cingular, parietal, and temporal fields. Second, each subregion mainly targeted distinct compartments within these association areas (Fig. S1L). In the following sections, we begin by approximating such patterns by mosaics of focal projections and then analyze weaker projections that were not well visible in this overlay.

Characterization of focal corticocortical projections

To characterize the 'focalness' of the corticocortical projections, we first identified 1867 'tracer foci' as the local maxima of tracer signals from all the datasets (Fig. S3A). The 3D patterns of their binarized images confirmed that they generally represent columnar extension with limited horizontal spread (Fig. S3B-E). Hierarchical clustering showed that each focus exhibited a variety of lamina preferences (Fig. 2A, 2B), whose distributions differed depending on the source-target combinations (Fig. S3F). Among them, we found statistically significant enrichment of the DL type in the dmPFC compared with dlPFCd and dlPFCv (Fig. 2C, one-way ANOVA, $p<0.05$). The original image suggests that this may reflect the widespread distribution of axon signals in layer 6 within the PFC (Fig. S3G, arrowheads). Comparison with the mouse data suggested that similar focal projections can be observed in mice only in a simpler form (Fig. S4).

Next, we examined the areal distribution patterns of tracer foci in detail (Fig. 2D-G). First, the number of foci per injection was significantly different between subregions within and outside the frontal areas, suggesting their different abilities to generate focal projections (Fig. 2E, one-way ANOVA, $p<0.05$). Second, each subregion targeted distinct compartments in the cingular, parietal, and temporal fields (Fig. 2D). Notably, all six PFC subregions had tracer foci in the cingular and temporal fields (note, however, that not all the injections had tracer foci in both fields; see supplementary text), whereas only limited subregions had tracer foci in the parietal field. As

schematically shown in Fig. S1L, there appear to be some topographic rules governing the extra-PFC projections. To test if we could quantify these rules, we used polynomial regression to predict the averaged positions of the tracer foci based on the injection coordinates (Fig. 2F, Fig. S5). Using this formula, the PFC map was transformed into skewed maps in the cingular and temporal fields, demonstrating retained topological relationships.

Regarding the parietal projections, we set the parietal region of interest as the seed to examine which of the available datasets project to this field. This analysis showed that the parietal projections are limited to the injections into the dorsolateral surface, including three PM injections plus one vlPFC injection field (Fig. 2G, right panel). Furthermore, the projections from the anterodorsal side (FP and dlPFCd) and the posteroventral side (dlPFCv and PM) were segregated into distinct compartments. Three injections that sit at the area border (indicated by X) had no parietal projections, suggesting the presence of abrupt borders (Fig. 2G, red arrows). Finally, we investigated the PFC projections to the lower order auditory areas (core and belt), considering the potential involvement of such connections in vocal communications(*18–20*). This analysis revealed bipartite projections from the anterior and posterior parts, which is reminiscent of a macaque study(*18*), proving the presence of auditory connections for the marmoset PFC (Fig. 2G, left panel).

Characterization of 'widespreadness' of corticocortical projections

The low-threshold logscale images of the tracer signals demonstrated that the tracer signals spread widely at low levels and even reached regions with no tracer foci (Fig. 3A, Fig. S6A), such as the perihippocampal gyrus (PHG) and higher-order visual areas (Vis) (e.g., dotted circles). An important consequence of such widespread projections is the extensive overlap between individual patterns. To find shared patterns of these tracer spreads, we applied the nonnegative matrix factorization (NMF) technique. Fig. 3B-E shows the result of NMF, which derived four components (or basis images) (NMF_W1–4) and the coefficients (coeff. 1–4) for the decomposition of the original image set. These four components represented commonly observed axes of variations. Overlaying them in pairs highlighted the distinctive features of these components (Fig. 3C, left panels). In one pair, NMF_W1 and NMF_W4 represented the dorsal and ventral spread, respectively, which is reminiscent of the macaque data(*3*).

The second pair, NMF_W2 and NMF_W3, closely resembled the antagonism of the 'apex transmodal network' versus 'canonical sensory-motor network' proposed by Buckner and Margulies(*21*), which may correspond to the default mode network and dorsal attention network, respectively(*22*). We found it notable that the projections to PHG and Vis (Fig. 3C, dotted circles) were segregated into NMF_W2 and W3. Thus, our NMF derived two previously proposed organizational schemes in an unsupervised and data-driven manner.

Next, we examined the coefficients of the NMF, which determine the spread pattern of each injection. As shown in Fig. 3D and 3E, different subregions showed characteristic coefficient profiles, which were statistically significant (one-way ANOVA, *; $p<0.05$). We found it important that the coefficients for NMF_W1 and NMF_W2 (coeff.1 and 2) show spectral contributions to the spread profiles of the six subregions and that the coeff. 1 vs coeff. 2 plot and the injection map (Fig. S6D) show similar topology. Thereby we used polynomial regression fitting and found good models to predict the coeff. 1 and 2 values based on the injection coordinates (Fig. S6D). Although coeff. 3 and 4 (for NMF_W3 and NMF_W4, respectively) did not show such gradients, they were also region-dependent. Thus, these coefficients are attributes of regional specificity, and the positional gradients in the PFC appear to dictate them.

Corticostriatal projections: focal and spread projections

Corticostriatal projections from the PFC play an integrative role in goal-directed behaviors. Beneath such integration lie complex interdigitations and overlaps of projections from different PFC subregions(*23*, *24*). Consistent with the macaque studies(*23*), we observed dense clumps of tracer signals surrounded by sparser and more widespread axonal signals, which all comprised fine axonal fibers with bouton-like varicosities (Fig. S7A and 7B). To determine the rules for the distributions of these tracer signals, we adopted strategies similar to those used for corticocortical projections. Fig. 4A and 4B shows typical examples of termination fields showing only strong (focal view) or widespread projections, including weak/sparse projections (logscale view).

In the focal view, we observed focal and patchy signals to align in rostrocaudal order within the caudate nucleus(*24*), except that A25 injection (#81) mostly targeted the nucleus accumbens (Fig. 4A, 'focal view'; see also Supplementary

Movie 3). In this view, we observed conspicuous subregion differences in two points. First, the extent of signal spread was highly variable across subregions; dlPFCv was the smallest, and dmPFC and ACC were the largest (Fig. 4C and 4D). Second, the positions of the rostrocaudally aligned foci varied systematically within the caudate nucleus, and we generally observed small overlaps of foci from adjacent subregions (Fig. 4E, Fig. S7C). To test if we could predict the averaged positions of tracer foci based on the topography of injections, we performed polynomial regression and obtained models that worked well for PFC injections, proving the importance of topography in determining the specificity of focal corticostriatal projections (Fig. S7D-G), consistent with previous macaque studies(*23*, *25*).

In the logscale view, we could visualize the diffusely spread nature of the corticostriatal projections(*23*) (Fig. 4B, 'logscale view'), which exhibited extensive overlaps (Fig. 4B, lower panel). To analyze these patterns, we performed NMF analyses and obtained four components (Fig. 4F and Fig. S7H). The coefficients of each subregion demonstrated that NMF_W2, 3, and 4 represented subregion-dominant domains for ACC, dlPFCv, and FP/OFC, respectively. On the other hand, NMF_W1 received projections from all PFC subregions. Thus, all the PFC subregions exert more or less significant effects on the caudate neurons, and all the striatal regions are influenced by some parts of the PFC. Interestingly, the profiles of these coefficient value sets looked similar to those of the corticocortical projections (Fig. 3E). Indeed, the scatter plots showed that these values are comparable as it is (for coeff. 1) or if we used the log-transformed (for coeff.2) or squared values (for coeff. 3 and 4). Spearman's rank correlation test (Fig. 4H) supported the significance of this similarity. These observations strongly suggest that the area-specific profiles of the corticocortical and corticostriatal projections are governed by the same PFC gradients, albeit in a nonlinearly skewed form.

Discussion

In this study, we performed high-resolution 3D mapping of the corticocortical and corticostriatal projections of the marmoset PFC and found two types of projections that may differentially affect the target area (Fig. S8). Focal-type projections converge densely on small populations of neurons in small target areas (indicated by green and

magenta circles). Spread-type projections, on the other hand, cover larger target areas with lower density. Instead, such projections are considered to exhibit extensive overlap in the target areas (shown by red and large arrows). This difference in connectivity suggests that focal-type projections cause efficient transmission via parallel point-to-point pathways, while spread-type projections are only effective when the activities of the macroscale networks are coordinated. The latter feature suggests that it may comprise the neural substrates of functional connectivity. In this regard, resting-state fMRI in marmosets extracted coactive networks involving frontal areas, including the candidates for the default mode network(*10*, *11*, *26*). It is hypothesized that psychotic symptoms of schizophrenia may be caused by the reduced influence of prior beliefs on the sensory data in Bayesian inference(*27*). Such a disease state may be explained by reduced macroscale functional connectivity of the PFC caused by chronic reduction or discordance of global PFC activities (Fig. S8, lower panel). Reduced default mode network activity in Alzheimer‘s disease(*28*) might be explained in the same way.

Neural recordings from the monkey PFC suggest that computations in the PFC emerge from the concerted dynamics of large populations of neurons(*29*), in which multidimensional activities may be superimposed(*30*). Although population coding does not need to be associated with particular anatomical structures (e.g., columns), the detailed features of the focal and spread projections revealed in this study may constrain how they are formed. For example, topographic connectivity(*18*, *23*, *24*, *31*, *32*) may lead to the topographic organization of functional properties(*33*, *34*) of PFC. The presence of various lamina types for focal projections is also likely to influence the interactions between the connected foci(*31*, *35*, *36*). When compared to mouse data (*5*, *6*), focal projections are characteristically observed in primates (Fig. S4) (*13–15*). We speculate that it may be a primate-specific strategy to cope with the high wiring cost of large brains(*17*). The raw images and standardized 3D data for the whole brain are available online from our Brain/MINDS data portal (Fig. S9; https://dataportal.brainminds.jp/marmoset-tracer-injection). Together with existing resources(*9*, *37*, *38*), our dataset will greatly advance our understanding of the primate brain, both from a basic and clinical perspective.

Methods

Marmoset experiments

All experimental procedures were carried out following the National Institute of Health Guide for the Care and Use of Laboratory Animals (NIH Publications No. 80-23) revised 1996 and the Japanese Physiological Society's "Guiding Principles for the Care and Use of Animals in the Field of Physiological Science," and were approved by the Experimental Animal Committee of RIKEN (W2020-2-009(2)). The age and sex of the marmoset used are listed in Table S1.

In our standard procedure, we performed MRI under anesthesia at least one week before surgery to plan injections. Surgery for tracer injection was performed as previously described with some modifications(*39*). Pressure injection was performed using a glass micropipette with an outer diameter of 25–30 μm connected to a nanoliter 2000 injector with a Micro4 controller (World Precision Instruments). For exposed cortical areas, we injected 0.1 μl each of tracers at two depths (0.8 and 1.2 mm from the surface) to deliver the AAV to the entire cortical layers. For deep injections (e.g., OFC), we injected 0.2 μl of tracers at one depth. With these volumes, we did not experience overflow, unlike the experience in our previous study(*39*). To avoid fluorescence cross-talk, all subjects received a fluorescent tracer at a single site. However, in some of our samples, we injected nonfluorescent tracers, such as BDA, into several other locations. After surgery, the marmosets were returned to the cages and sacrificed four weeks later.

AAV tracers

We used a TET system to amplify fluorescence signals(*40–42*). Our standard tracer mix included AAV1-Thy1S-tTA (1 × 10e9 vg/μL), AAV1-TRE-clover (1 × 10e9 vg/μL; a GFP derivative), and AAV1-TRE3-Vamp2-mTFP1 (0.25 × 10e9 vg/μL; cyan fluorescent protein targeted to the pre-synapse). In later experiments, we also mixed AAV2retro EF1-Cre (1.5 × 10e9 vg/μL) with the tracer mix for co-injection. We deposited plasmids for these AAV vectors to Addgene (https://www.addgene.org/).

PFC injections

In this study, we present the data of 44 high-quality datasets that were injected into various frontal areas (Fig. 1F, Fig. S1J, and Table S1), referring to previous studies (*37*, *43–46*). We divided the frontal areas of marmoset into nine subregions, including the frontopolar cortex (FP), dorsolateral PFC_ventral (dlPFCv), dorsolateral PFC_dorsal

297 (dlPFCd), dorsomedial PFC (dmPFC), ventrolateral PFC (vlPFC), anterior cingulate
298 cortex (ACC), orbitofrontal cortex (OFC), as well as premotor areas (PM) and dorsal
299 ACC (dACC) (Fig. S1J). The ACC subregion in this study comprises areas A32, A14,
300 A25, and A24a and corresponds to the subgenual anterior cingulate cortex (sgACC) and
301 perigenual ACC (pgACC) in other studies(*47*) and was differentiated from the dACC
302 comprising A24b and A24c. We injected most densely into dlPFC, which were further
303 subdivided into "dlPFCv" and "dlPFCd," corresponding to the areas 8aV/A45 and
304 8aD/46D, respectively, by our cortical annotation; dlPFCv most likely corresponds to
305 the "frontal eye field (FEF) (*21*, *48*)." The correspondence of "dlPFCd" with macaque
306 areas 46, 9/46, and 8aD is currently unclear. However, our results suggest inclusion of
307 A46-like areas in dlPFCd, judging from the auditory projection (Fig. 2G). Throughout
308 the manuscript, we used 29 datasets with clean injections in six PFC subregions (FP,
309 dmPFC, dlPFCd, dlPFCv, ACC, and OFC) for subregion comparison. These injections
310 are shown color-coded in Fig. 1F and Fig. S1J. Some of the injections localized at the
311 border of these subregions and were used only for annotation-free analyses (gray dots in
312 Fig. 1F). Injections into the vlPFC, PM, and dACC subregions were also used only for
313 the selected analyses.
314
315 **Serial two-photon tomography imaging (STPT)**
316 After transcardial perfusion with 4% paraformaldehyde in 0.1 M phosphate buffer (pH
317 7.4), the marmoset brains were retrieved, post-fixed at 4 °C for 2–3 days, and
318 transferred to 50 mM phosphate buffer (pH 7.4). All marmoset brains were subjected to
319 *ex vivo* MRI before further processing. Agarose embedding was performed as
320 previously described(*4*) in 5 % agarose using a custom-made mold. Before embedding,
321 we treated the brain with 1 mg/ml collagenase (Wako 031-17601) at 37 °C for one hour
322 and manually removed the meninges as thoroughly as possible. This step ensured direct
323 crosslinking of agarose to the brain for stable sectioning at a 50-µm interval. STPT was
324 performed as described(*4–6*) using TissueCyte1000 or TissueCyte1100 (TissueVision).
325 We immersed the agarose block in 50 mM PB supplemented with 0.02 % sodium azide
326 for imaging and sectioning. We used a 940 nm laser for excitation, and the two-photon
327 excited fluorescence was recorded in three-color channels. Three-color imaging was
328 critical in our study to (1) distinguish lipofuscin granules from tracers, which are
329 characteristic of aged brain(*49*) (Fig. S1G) and (2) to delineate AAV-infected cell bodies

330 around the injection site, which was only possible in the unsaturated blue channel (ch3
331 Fig. S1D). In our setup, the resolutions for x and y were 1.385 μm/pixel and 1.339
332 μm/pixel, respectively. Both hemispheres were processed in the rostral-to-caudal
333 direction (coronal). We imaged four optical planes (12 μm intervals) per 50 μm slice for
334 the rostral part and one optical plane per slice for the caudal part. We used only the first
335 optical plane in this study. One run consisted of 20–30 sessions with different XY
336 coverage and took approximately 10 days to process the whole brain.
337
338 **Post-STPT histology**
339 Sliced tissue sections were manually collected for further histological analysis. To
340 confirm the cytoarchitecture, we collected one in ten sections for Nissl staining. The
341 floating sections were mounted onto a glass slide after the agarose was removed.
342 Mounted sections were rehydrated with PBS, and dark-field backlit images were taken
343 using an all-in-one microscope (Keyence BZ-X710) before Nissl staining. The backlit
344 image showed myelination patterns that were very similar to conventional myelin
345 staining (manuscript in preparation). We used the same section for Nissl staining, and
346 the combined information of the backlit and Nissl-images provided useful information
347 for anatomical delineation (Fig. S2).
348 For confocal microscopic observations, we stained the retrieved sections with an
349 anti-GFP antibody (Abcam, ab13790) in conjunction with Alexa488 conjugated anti-
350 chick antibody. After mounting on a glass slide, the stained sections were imaged using
351 an Olympus Fluoview FV3000 confocal microscopy using a 40× silicone immersion
352 lens (UPLSAPO40XS).
353
354 **Image processing pipeline**
355 The details of the image processing pipeline are described elsewhere(*50*). Briefly, the
356 raw images in the three channels were stitched after background correction. The Ch1
357 (red) image provided the tissue background image with some tracer bleed-through, and
358 the Ch2 (green) image provided the tracer fluorescence and tissue background. In our
359 setup, we observed very weak signals for Ch3 (blue), which helped identify AAV-
360 transduced cell bodies that were impossible with other channels due to signal saturation.
361 Using this information, the pipeline determined the exact spread of AAV transduction
362 without human intervention. The pipeline also accurately segmented the axon signals

363 from the background based on the Ch1 and Ch2 images. On visual inspection, we
364 encountered almost no false positives for this segmentation. The detection was quite
365 sensitive, although it was usually partial. The stitched coronal section slices (more than
366 600) were placed in the 3D space based on the recorded stage coordinates and registered
367 to the standard reference space or STPT template (see below). In this data
368 transformation, a unit isocube corresponds to a 50 μm × 50 μm square of one slice
369 image (50 μm interval), whose signal intensity was determined by the sum of positive
370 pixels, each of which was weighted for fluorescent intensity. In this way, we secured a
371 wide dynamic range of quantification and a high signal-to-noise ratio. All quantitation
372 was based on the fluorescence-weighted segmentation values.
373 The total sum of thus-defined signal intensities was highly variable between
374 samples due to various experimental causes, including the differential spread of the
375 tracer at injection. However, there was little correlation with age ($r = -0.062$; $p = 0.69$)
376 or sex ($p = 0.38$, by the t-test), which we did not distinguish in the current study.
377
378 **Standard reference space (STPT template)**
379 To facilitate 3D-3D registration, we built a standard reference image for a marmoset
380 brain based on iteratively averaged Ch1 images (manuscript in preparation). We call this
381 50 μm-isocubic 3D image as the "STPT template." To allow multimodal data
382 integration, the initial averaging step was performed using BMA2019 Ex Vivo (Space
383 2), which is a 100 μm isocubic reference image based on a population average of 25 *ex*
384 *vivo* MRI (T2) contrasts(*51*). Nissl-based cortical annotation originally performed on a
385 single brain(*52*, *53*) was transferred to the STPT template and used without further
386 adjustment.
387
388 **Handling of 3D data for visualization and substructure analyses**
389 After completion of the pipeline, the tracer intensity data and AAV-transduced area data
390 were converted to the STPT template-registered form. These 3D data became available
391 in a NIFTI format (https://nifti.nimh.nih.gov/), and the substructure of interest could be
392 easily excised for each sample using the labelmap. The labelmap for the definition of
393 substructures was manually annotated based on the image contrast of the STPT template
394 (Fig. S1A). After the excision of the substructure of interest, the tracer intensities were
395 standardized to the maximum value within the substructure, converted to 8-bit or 16-bit,

and saved as a tiff stack file. FluoRender(*54*) was used to visualize 3D data for the presentation of images and movies. Striatal data sometimes included strong contaminating signals of passing axon fibers within the internal capsule and white matter. In such cases, we manually masked these regions using a 3D Slicer (https://www.slicer.org/) and performed the normalization again.

Conversion of cortex data into a flatmap stack and its normalization

The outer and inner surfaces of the cerebral cortex were defined based on the image intensity of the STPT template and manually corrected when necessary. Vertices connecting the outer and inner surfaces (Fig. S1B, right side) were used to extend the midpoint flatmap(*51*) to include lamina information (Fig. S1B, left side)(*50*). To standardize the intensities of the corticocortical projection patterns of the flatmap stack, we prioritized the constancy of signals in the upper parts (layer level 26–50) because the lower layers contained more diffuse and widespread signals, some of which could be passing fibers. We also knew that the signal levels of the tracers at the injection site are unreliable due to fluorescence saturation. Therefore, we first averaged layer level 26–50 of the flatmap stack and masked the injection area based on the MIP of all layers of the injection flatmap stack. We then selected pixels with the top 0.1% of the intensity values from the rest and set the minimum value of the selected pixels at 10,000. This standardization method provided very similar patterns across different intensity ranges within the same frontal group irrespective of the original tracer intensity. The same coefficient was used to standardize the flatmap stack. For the six-color overlay of different PFC groups in Fig. 1G, the MIP images for layer level 26–50 from the same PFC subregions were MIP-merged. The flatmaps of different groups were then overlaid with different colors in a “winner-take-all” style, in which the color of the strongest signals was displayed to avoid color mixing. For the six-color overlay in Fig. S1K, the color was simply merged when overlapped.

To convert the tracer intensity data into the logscale, the standardized values were log-transformed after adding 0.001 and thresholded by 0. For visualization, the log-transformed data were scaled to a representation in 8-bit.

Detection and characterization of tracer foci in corticocortical projections

Tracer foci were detected as local maxima in 2D. Local maxima in 2D were identified

using the “find peaks” function of MATLAB 2019a, inspired by the Fast 2D peak finder(*55*) (https://www.mathworks.com/matlabcentral/fileexchange/37388-fast-2d-peak-finder), MATLAB Central File Exchange. Briefly, the 2D image was Gaussian smoothed, and the peaks larger than the defined minimum height values were searched in the x- and y-directions, pixel by pixel. Only the 2D spots that peaked in both the x- and y-direction searches were identified as local maxima. To detect tracer foci in corticocortical projections, we used the upper layer-averaged (layer level 26–50), injection site masked, and standardized flatmap to find local maxima in 2D, as described above. The minimum height value for tracer foci detection was set at 100, which is two orders of magnitude lower than the standardization value of 10,000. Tracer foci detected at the fringe of the injection site due to masking were removed manually by visual inspection. We detected 1867 tracer foci from 44 datasets.

To examine the extent of convergence of tracer signals to the centers of tracer foci, we set two ROIs for measurement that surround the foci centers (Fig. S3C). One was a 19 × 19 × 50 pixel cuboid, and the other was a cylinder with a 4-pixel radius. The idea is to measure the ratio of the number of tracer-positive voxels contained within the cylinder to that in the cuboid. First, we standardized the intensity of the tracer signals by the maximum value within the upper half of the central cylinder. Second, the tracer signals were binarized at 0.5, that is, half the maximum value. Third, the largest clump of the binarized tracer signals within the upper half of the central cylinder was chosen to represent the tracer focus of choice (Fig. S3C, right panel, red clump). The ratio of the number of voxels contained within the central cylinder to that of all voxels that constitute this binary clump was calculated as the index of central convergence. Tracer foci were often clustered, and stronger tracer signals at nearby locations connected to the central clump. Therefore, we classified the tracer foci into InPeak (InP) and OutPeak (OutP) groups, based on whether the maximum value within the upper cylinder ROI (MAXin) is higher or lower than the outside maximum (MAXout) (Fig. S3D). We expected that the InPeak group would have less interference from the neighboring foci than the OutPeak group. The ratio of central convergence for the InPeak group reached 87 ± 19%, and that for the OutPeak group was 55 ± 33%. The vertical continuity measured by the height of the binary clumps was 21 ± 13 and 32 ± 16 pixels for the InPeak and OutPeak groups, respectively. Combined, these data indicate an overall “columnar” distribution of the detected tracer foci to localize within the central cylinder

with a 4-pixel radius, consistent with the reported submillimeter size in macaques and squirrel monkeys(*13*).

Inspection of signal distributions for individual tracer foci indicated various lamina preferences for these foci. Because the directions of the axonal extension were not always perpendicular to the flatmap and often tilted, we measured the maximum intensity of tracer signals within the central cylinder for each of the 50 layers and defined it as the lamina profile of the tracer focus of interest. To classify the lamina profiles of the 1867 tracer foci, we performed hierarchical clustering. Pearson's correlation coefficient was used to measure distance, and Ward's method was used for unsupervised clustering. Although we selected tracer foci based on the values of layer level 26–50, the profiles of all 50 layers were used to calculate the correlation coefficient. Fig. 2A shows the original lamina profiles of the tracer foci (before averaging) aligned according to the tree structure. We divided them into eight clusters (separated by white border lines) and averaged each of the lamina profiles shown in Fig. 2A. We defined three lamina types, "DL," "ML", and "UL," based on the tree level that generates three clusters. The defined lamina types were color-coded blue, green, and red, respectively, to be presented in flatmap form in Fig. S3F.

We noticed that our injections were not always evenly distributed across layers and were sometimes biased. Considering the presence of lateral projections in the primate PFC(*15*), it is possible that the depth of injection affects the lamina preferences of the tracer foci. To test this possibility, we examined the relative abundance of injection volumes in the five lamina compartments for each sample (Fig. S3H) and tested whether there was any correlation between injection depth and lamina profiles. The ratio of DL types among all tracer foci indeed showed a moderate correlation ($r = 0.49$; $p = 8.2 \times 10e\text{-}4$) with the ratio of volume in the deep layers (1–20) among all volumes for each injection. However, when we subtracted this effect for ANOVA, we found significant differences between dlPFCd and dmPFC (Tukey's test, $p = 0.0091$).

Comparison of mouse and marmoset data for focal projections.

All the mouse data used in this study were obtained from Mouse Brain Connectivity Atlas (https://connectivity.brain-map.org/). First, we selected the datasets with injections into the frontal areas (ACAd, ACAv, FRP, ILA, MOs, ORBI, ORBm, ORBvl, PL) of the wild-type mice (Table S2). The whole-brain tracer data (projection energy)

with 10 μm resolution for these datasets were then acquired via the application programming interface (API) and converted to flatmaps as previously described(*56*). The flatmaps for both hemispheres were resized to 816x408 pixels and the image intensity was standardized similarly to that used for the marmoset flatmap except that the injection center was not excised prior to measurement. Detection of the tracer foci was performed using the same code used for the marmoset flatmap. The mouse flatmaps represented the average of all layers, whereas the marmoset analysis used flatmaps representing only the upper half of the layers. To compare with the mouse data, we performed a new foci detection using the flatmaps of all layers (Fig. S4E and F).

Our detection algorithm simply finds the peaks above a threshold in the X and Y directions after smoothing. It can therefore detect broad peaks that appear different from "focal" projections of the marmoset cortex. It is also sensitive to standardization methods. The mouse data differ from our marmoset data in several ways. (1) The mouse study used regular AAV-GFP, which is less efficient at labeling axons than our TET-enhanced AAV. (2) Mouse brains were sliced at 100 μm intervals as opposed to 50 μm intervals in our data, which is less reliable in detecting submillimeter scale structures. (3) The frontal region of the mouse is curved, and flatmapping results in very large distortions. (4) We could not subtract the tracer signals of the cell bodies before standardization for the mouse data. All these differences could lead to differences in the detection of the tracer foci in the two species. However, the original slice images suggest that the projection patterns of axons are very different between mice and marmosets (e.g., Fig. S4A, B). Therefore, the quantitative estimation in Fig. S4F is considered to be legitimate overall.

Prediction of tracer foci distribution patterns by polynomial regression for corticocortical projections.

To examine the topographic projections to the cingular and temporal fields, we set the ROIs for these areas, as shown in Fig. S5A, and determined the center of mass of the tracer foci present within these ROIs for each sample for the six PFC subregions. Among the 29 injections, 24 had at least one tracer foci in the cingular field, and 21 had tracer foci in the temporal field. To find a regression model to predict the projection from the injection, we used a polynomial regression of degree 2. As predictor variables, we used the X and Y coordinates of the injection center in the flatmap, and as response

variables, we used the X or Y coordinates of the averaged positions of tracer foci in the cingular and temporal ROIs. As shown in Fig. S5B and C, we achieved reasonable fitting (R^2 =0.68~0.92) for the injections in the PFC. The permutation test confirmed the statistical significance of these predictions. To extrapolate the obtained topography, we calculated the projections from every point in the PFC map to the cingular and temporal fields, as shown in Fig. S5D. This calculation resulted in projections outside the flatmap, suggesting the presence of distortions at the fringes. Fig. S5D displays only the projections within the flatmap region.

Non-negative matrix factorization (NMF) analyses of corticocortical and corticostriatal projection patterns

To find common patterns of projections for corticocortical (or corticostriatal) projection, we performed NMF analyses using log-transformed data. NMF has recently been used as an effective method of dimensionality reduction for neuroimaging(*57*). Unlike principal component analysis, all coefficients and basis images are nonnegative, allowing easier interpretation of the data(*58*). For corticocortical projections, 500 × 500 pixel MIPs of all layers with injection site masks were downsized to 100 × 100 pixel size and the data for 44 injections were converted to 44 × 10,000 matrix to be used for "nnmf" function of MATLAB. For corticostriatal projections, a 180 × 300 × 220 voxel space containing the left striatum was downsized to a 45 × 75 × 55 space, and a 44 × 185,625 matrix was used for NMF analyses. NMF analysis attempts to decompose the original matrix A (sample × pattern) into basis images (or components) W and coefficients H (A ≅ WH). Due to the nonnegative constraints, A is not exactly equal to WH. Furthermore, the nnmf function of MATLAB uses an iterative algorithm starting with random initial values for W and H, and the results obtained vary slightly each time. To find the best result, we repeated the analyses 100 times and examined the residuals between A and WH. The residuals were relatively constant but sometimes became large. Inspection of the basis images showed that very similar images were generated when the residuals were small. Therefore, we selected W and H with the least residuals as the basis images. In this analysis, the number of basis images was determined empirically. Because we had only 44 datasets for analysis, we tried to minimize the number of basis images while achieving sufficient reconstitution efficiency. With four basis images, the averaged correlation coefficients between the reconstituted and the original images was

approximately 0.93 (Fig. S6C).

Because we observed similarities between the injection positions and coeff. 1 vs. coeff. 2 map, we tested whether these coefficients could be predicted based on the injection coordinates. We used a polynomial regression model of degree 3 to find the optimal fits, as shown in Fig. S6D.

Occupancy and colocalization of focal tracer signals in the striatal region

We noticed that the occupancy of tracer signals in the striatal regions varied widely among the PFC subregions when strong/focal projections were visualized (Fig. 4A, focal view). To quantitatively estimate this point, we set the threshold at 50% of the maximum intensity (Fig. 4C) and counted the ratio of positive voxels in the caudate nucleus, putamen, and nucleus accumbens, separately over the entire striatal voxels for each sample. For comparison of the six PFC subregions, the values in the three striatal compartments were summed for analysis by ANOVA. For the colocalization analysis, the ratio of the overlapping voxel numbers to the number of combined voxels was calculated for every pair of 29 injections (Fig. S7C). Due to patchy distributions, overlaps within the same PFC subregions were not necessarily high and varied greatly among pairs.

Detection of tracer foci for corticostriatal projections in 3D

For the detection of tracer foci for corticostriatal projections in 3D, the 3D data were first converted to a set of XY and YZ MIP images for detection of local maxima in each 2D image in a similar way used for the detection of corticocortical tracer foci, and the 3D positions that can explain both MIP images were selected as the local maxima in 3D. When two foci were detected within a six-pixel distance in 3D, we combined them for simplicity. The detected foci were projected onto the XY, YZ, and XZ MIP images for visual inspection for accurate detection. In the detection of caudate tracer foci, we found that strong signals in the Muratov bundle or internal capsule were sometimes included and selected as tracer foci. In such cases, we either masked those regions for re-standardization or simply deselected those foci. Tracer intensities were standardized to the maximum values within the striatal region for each sample, and the minimum height value for tracer foci detection was set at half the maximum value. An example of such foci detection is shown in Fig. S7D. The distribution of these foci could generally be

well approximated by an elongated ellipsoid (Fig. S7D, red ellipses), consistent with the previous observation that macaque corticostriatal projections are longitudinally aligned(*24*).

Prediction of tracer foci distribution patterns by polynomial regression model for corticostriatal projections

To find regression models that can predict the projection coordinates from the injection coordinates, we tested polynomial regression model with degree 2 and searched for the optimal fit. As predictor variables, we used the x, y, and z coordinates of injections in the STPT template space. As response variables, we used the x, y, or z coordinates for the average positions of the detected tracer foci within the caudate nucleus. To visualize the transformation of the coordinates using these models, we drew five lines in the frontal cortex of the STPT template to represent the coronal planes at 20-px intervals that roughly correspond to AP = +13.5, +14.5, +15.5, +16.5, and +17.5 in the Paxinos atlas(*43*) and visualized the corresponding lines in the caudate.

Statistical tests

Values are reported as mean ± standard deviation (SD). The correlation coefficients (r) in Fig. S3I and Fig. S6C refer to the Pearson correlation. Those in Fig. 4H refer to Spearman's rank correlation. R^2 for the regression model refers to the coefficients of determination. The p-values were calculated using one-way ANOVA and Tukey's post hoc test for significant factors in the ANOVA.

Acknowledgments:

We thank Y. Hasegawa and RIKEN ARD for marmoset care. We thank the RIKEN CBS-Olympus Collaboration Center for the technical assistance with confocal image acquisition.

Funding: Supported by Scientific Research on Innovative Areas (22123009) from MEXT, Japan, and by the program for Brain Mapping by Integrated Neuro technologies for Disease Studies (Brain/MINDS: JP22dm0207001 to T.Y. and JP22dm0207088 to K.N.) from AMED, Japan.

Author contributions: A.W. and T.Y. designed the study. A.W. and J.W. performed

animal surgery, serial two-photon tomography, post-imaging histology, and manual data curations. H.S. constructed the automatic image processing pipeline. A.W., M.T and H.M. designed and prepared the AAV vector system. A.W., H.S., K.N., S.I., H.A. and N.I. analyzed the data. Al.W. and R.G. constructed the data viewers and contributed to flatmap generation. J.H. and H.O. performed MRI. A.W. wrote the paper with comments from all other authors.

Competing interests: All authors declare no competing interests.

Data availability

Data (including high-resolution images, segmentation, and registration of the STPT template) are available through the Brain/MINDS data portal (https://dataportal.brainminds.jp/ [Temporary address for review purpose https://dataportal.brainminds.jp/marmoset-tracer-injection]). The high-resolution images used in the paper are labeled with marmoset number and section number (e.g., #82-139) and are available through the zoomable section viewer. The flatmap data for the cortical projections are available from the flatmap viewer. The experimental details associated with each dataset can be retrieved from the metadata section. In addition to the visualization and search tools available at these sites, users can download standardized 3D data for tracer segmentation, fluorescence-weighted segmentation, AAV-transduced cell segmentation, and original and standardized flatmap stack data in nifti format on request. The STPT template and the associated substructure labelmap are also available from our data portal (https://dataportal.brainminds.jp/). The codes used in the current study are available upon request.

651 **Supplementary Text**

652 Probabilistic nature of tracer foci distribution in the cerebral cortex

653 We have shown that the average positions of tracer foci are defined by the positional
654 gradients within the PFC (Fig. 2F) and that the number of foci per injection depends on
655 the PFC area (Fig. 2E). However, the actual distribution patterns of the tracer foci are
656 currently unpredictable. Of the 44 injections, 35 and 29 had at least one (quite often
657 multiple) tracer foci in the cingular and temporal fields, respectively, and 21 injections
658 had tracer foci in both. Although all six PFC subregions had connections to the cingular
659 and temporal fields as a whole, not all locations within the subregions were connected
660 to both fields. We suggest that the positional gradients in the PFC only determine the
661 trends of projections to the three association fields, and whether and where the focal
662 connectivities are established is probabilistically determined. In this regard, the tracer
663 foci from eight injections into the dlPFCv are scattered over the parietal field, as shown
664 in Fig. 2D. Although these foci targeted similar locations within the parietal field, the
665 number of tracer foci per area differed from sample to sample, which may reflect the
666 probabilistic nature of the focal projections.
667
668
669

References

1. J. M. Fuster, *The prefrontal cortex* (Elsevier/AP, Academic Press is an imprint of Elsevier, Amsterdam ; Boston, Fifth edition., 2015).
2. S. N. Haber, H. Liu, J. Seidlitz, E. Bullmore, Prefrontal connectomics: from anatomy to human imaging. *Neuropsychopharmacology* (2021), doi:10.1038/s41386-021-01156-6.
3. D. N. Pandya, B. Seltzer, M. Petrides, P. B. Cipolloni, *Cerebral cortex: architecture, connections, and the dual origin concept* (Oxford University Press, Oxford, 2014).
4. T. Ragan, L. R. Kadiri, K. U. Venkataraju, K. Bahlmann, J. Sutin, J. Taranda, I. Arganda-Carreras, Y. Kim, H. S. Seung, P. Osten, Serial two-photon tomography for automated ex vivo mouse brain imaging. *Nat Methods*. **9**, 255–258 (2012).
5. J. A. Harris, S. Mihalas, K. E. Hirokawa, J. D. Whitesell, H. Choi, A. Bernard, P. Bohn, S. Caldejon, L. Casal, A. Cho, A. Feiner, D. Feng, N. Gaudreault, C. R. Gerfen, N. Graddis, P. A. Groblewski, A. M. Henry, A. Ho, R. Howard, J. E. Knox, L. Kuan, X. Kuang, J. Lecoq, P. Lesnar, Y. Li, J. Luviano, S. McConoughey, M. T. Mortrud, M. Naeemi, L. Ng, S. W. Oh, B. Ouellette, E. Shen, S. A. Sorensen, W. Wakeman, Q. Wang, Y. Wang, A. Williford, J. W. Phillips, A. R. Jones, C. Koch, H. Zeng, Hierarchical organization of cortical and thalamic connectivity. *Nature*. **575**, 195–202 (2019).
6. S. W. Oh, J. A. Harris, L. Ng, B. Winslow, N. Cain, S. Mihalas, Q. Wang, C. Lau, L. Kuan, A. M. Henry, M. T. Mortrud, B. Ouellette, T. N. Nguyen, S. A. Sorensen, C. R. Slaughterbeck, W. Wakeman, Y. Li, D. Feng, A. Ho, E. Nicholas, K. E. Hirokawa, P. Bohn, K. M. Joines, H. Peng, M. J. Hawrylycz, J. W. Phillips, J. G. Hohmann, P. Wohnoutka, C. R. Gerfen, C. Koch, A. Bernard, C. Dang, A. R. Jones, H. Zeng, A mesoscale connectome of the mouse brain. *Nature*. **508**, 207–214 (2014).
7. H. Okano, Current Status of and Perspectives on the Application of Marmosets in Neurobiology. *Annu Rev Neurosci*. **44**, 27–48 (2021).
8. J. F. Mitchell, D. A. Leopold, The marmoset monkey as a model for visual neuroscience. *Neurosci Res*. **93**, 20–46 (2015).
9. C. Liu, F. Q. Ye, J. D. Newman, D. Szczupak, X. Tian, C. C.-C. Yen, P. Majka, D. Glen, M. G. P. Rosa, D. A. Leopold, A. C. Silva, A resource for the detailed 3D mapping of white matter pathways in the marmoset brain. *Nat Neurosci*. **23**, 271–280 (2020).
10. C. Liu, C. C.-C. Yen, D. Szczupak, F. Q. Ye, D. A. Leopold, A. C. Silva, Anatomical and functional investigation of the marmoset default mode network. *Nat Commun*. **10**, 1975 (2019).

11. Y. Hori, D. J. Schaeffer, A. Yoshida, J. C. Cléry, L. K. Hayrynen, J. S. Gati, R. S. Menon, S. Everling, Cortico-Subcortical Functional Connectivity Profiles of Resting-State Networks in Marmosets and Humans. *J Neurosci*. **40**, 9236–9249 (2020).
12. A. Uematsu, J. Hata, Y. Komaki, F. Seki, C. Yamada, N. Okahara, Y. Kurotaki, E. Sasaki, H. Okano, Mapping orbitofrontal-limbic maturation in non-human primates: A longitudinal magnetic resonance imaging study. *Neuroimage*. **163**, 55–67 (2017).
13. N. M. Bugbee, P. S. Goldman-Rakic, Columnar organization of corticocortical projections in squirrel and rhesus monkeys: similarity of column width in species differing in cortical volume. *J Comp Neurol*. **220**, 355–364 (1983).
14. M. L. Pucak, J. B. Levitt, J. S. Lund, D. A. Lewis, Patterns of intrinsic and associational circuitry in monkey prefrontal cortex. *J Comp Neurol*. **376**, 614–630 (1996).
15. J. B. Levitt, D. A. Lewis, T. Yoshioka, J. S. Lund, Topography of pyramidal neuron intrinsic connections in macaque monkey prefrontal cortex (areas 9 and 46). *J Comp Neurol*. **338**, 360–376 (1993).
16. N. T. Markov, P. Misery, A. Falchier, C. Lamy, J. Vezoli, R. Quilodran, M. A. Gariel, P. Giroud, M. Ercsey-Ravasz, L. J. Pilaz, C. Huissoud, P. Barone, C. Dehay, Z. Toroczkai, D. C. Van Essen, H. Kennedy, K. Knoblauch, Weight consistency specifies regularities of macaque cortical networks. *Cereb Cortex*. **21**, 1254–1272 (2011).
17. D. S. Bassett, E. T. Bullmore, Small-World Brain Networks Revisited. *Neuroscientist*. **23**, 499–516 (2017).
18. L. M. Romanski, B. Tian, J. Fritz, M. Mishkin, P. S. Goldman-Rakic, J. P. Rauschecker, Dual streams of auditory afferents target multiple domains in the primate prefrontal cortex. *Nat Neurosci*. **2**, 1131–1136 (1999).
19. M. Medalla, H. Barbas, Specialized prefrontal “auditory fields”: organization of primate prefrontal-temporal pathways. *Front Neurosci*. **8**, 77 (2014).
20. S. J. Eliades, C. T. Miller, Marmoset vocal communication: Behavior and neurobiology. *Dev Neurobiol*. **77**, 286–299 (2017).
21. R. L. Buckner, D. S. Margulies, Macroscale cortical organization and a default-like apex transmodal network in the marmoset monkey. *Nat Commun*. **10**, 1976 (2019).
22. R. L. Buckner, L. M. DiNicola, The brain’s default network: updated anatomy, physiology and evolving insights. *Nat Rev Neurosci*. **20**, 593–608 (2019).
23. S. N. Haber, K.-S. Kim, P. Mailly, R. Calzavara, Reward-related cortical inputs define a large striatal region in primates that interface with associative cortical connections,

providing a substrate for incentive-based learning. *J Neurosci*. **26**, 8368–8376 (2006).

24. L. D. Selemon, P. S. Goldman-Rakic, Longitudinal Topography and lnterdigitation of Corticostriatal Projections in the Rhesus Monkey'. *The Journal of Neuroscience*. **5**, 19 (1985).
25. B. B. Averbeck, J. Lehman, M. Jacobson, S. N. Haber, Estimates of projection overlap and zones of convergence within frontal-striatal circuits. *J Neurosci*. **34**, 9497–9505 (2014).
26. Y. Hori, J. C. Cléry, J. Selvanayagam, D. J. Schaeffer, K. D. Johnston, R. S. Menon, S. Everling, Interspecies activation correlations reveal functional correspondences between marmoset and human brain areas. *Proc Natl Acad Sci U S A*. **118**, e2110980118 (2021).
27. R. B. Rutledge, R. A. Adams, in *Computational Models of Brain and Behavior* (John Wiley & Sons, Ltd.).
28. M. D. Greicius, G. Srivastava, A. L. Reiss, V. Menon, Default-mode network activity distinguishes Alzheimer's disease from healthy aging: evidence from functional MRI. *Proc Natl Acad Sci U S A*. **101**, 4637–4642 (2004).
29. V. Mante, D. Sussillo, K. V. Shenoy, W. T. Newsome, Context-dependent computation by recurrent dynamics in prefrontal cortex. *Nature*. **503**, 78–84 (2013).
30. M. Rigotti, O. Barak, M. R. Warden, X.-J. Wang, N. D. Daw, E. K. Miller, S. Fusi, The importance of mixed selectivity in complex cognitive tasks. *Nature*. **497**, 585–590 (2013).
31. H. Barbas, General Cortical and Special Prefrontal Connections: Principles from Structure to Function. *Annu. Rev. Neurosci*. **38**, 269–289 (2015).
32. E. Borra, C. G. Ferroni, M. Gerbella, V. Giorgetti, C. Mangiaracina, S. Rozzi, G. Luppino, Rostro-caudal Connectional Heterogeneity of the Dorsal Part of the Macaque Prefrontal Area 46. *Cereb Cortex*. **29**, 485–504 (2019).
33. M. R. Riley, X.-L. Qi, X. Zhou, C. Constantinidis, Anterior-posterior gradient of plasticity in primate prefrontal cortex. *Nat Commun*. **9**, 3790 (2018).
34. J. M. Huntenburg, P.-L. Bazin, D. S. Margulies, Large-Scale Gradients in Human Cortical Organization. *Trends Cogn Sci*. **22**, 21–31 (2018).
35. D. J. Felleman, D. C. Van Essen, Distributed hierarchical processing in the primate cerebral cortex. *Cereb Cortex*. **1**, 1–47 (1991).
36. J. Vezoli, M. Vinck, C. A. Bosman, A. M. Bastos, C. M. Lewis, H. Kennedy, P. Fries, Brain rhythms define distinct interaction networks with differential dependence on anatomy. *Neuron*, S0896-6273(21)00725-X (2021).
37. P. Majka, S. Bai, S. Bakola, S. Bednarek, J. M. Chan, N. Jermakow, L. Passarelli, D. H.

Reser, P. Theodoni, K. H. Worthy, X.-J. Wang, D. K. Wójcik, P. P. Mitra, M. G. P. Rosa, Open access resource for cellular-resolution analyses of corticocortical connectivity in the marmoset monkey. *Nat Commun*. **11**, 1133 (2020).

38. X.-J. Wang, U. Pereira, M. G. Rosa, H. Kennedy, Brain connectomes come of age. *Curr Opin Neurobiol*. **65**, 152–161 (2020).
39. A. Watakabe, M. Ohtsuka, M. Kinoshita, M. Takaji, K. Isa, H. Mizukami, K. Ozawa, T. Isa, T. Yamamori, Comparative analyses of adeno-associated viral vector serotypes 1, 2, 5, 8 and 9 in marmoset, mouse and macaque cerebral cortex. *Neurosci Res*. **93**, 144–157 (2015).
40. O. Sadakane, A. Watakabe, M. Ohtsuka, M. Takaji, T. Sasaki, M. Kasai, T. Isa, G. Kato, J. Nabekura, H. Mizukami, K. Ozawa, H. Kawasaki, T. Yamamori, *eNeuro*, in press, doi:10.1523/ENEURO.0019-15.2015.
41. A. Watakabe, M. Takaji, S. Kato, K. Kobayashi, H. Mizukami, K. Ozawa, S. Ohsawa, R. Matsui, D. Watanabe, T. Yamamori, Simultaneous visualization of extrinsic and intrinsic axon collaterals in Golgi-like detail for mouse corticothalamic and corticocortical cells: a double viral infection method. *Front Neural Circuits*. **8**, 110 (2014).
42. H. Hioki, E. Kuramoto, M. Konno, H. Kameda, Y. Takahashi, T. Nakano, K. C. Nakamura, T. Kaneko, High-level transgene expression in neurons by lentivirus with Tet-Off system. *Neurosci Res*. **63**, 149–154 (2009).
43. G. Paxinos, C. Watson, M. Petrides, M. Rosa, H. Tokuno, *The marmoset brain in stereotaxic coordinates* (Academic Press, London; Waltham, MA, 2012).
44. A. C. Roberts, D. L. Tomic, C. H. Parkinson, T. A. Roeling, D. J. Cutter, T. W. Robbins, B. J. Everitt, Forebrain connectivity of the prefrontal cortex in the marmoset monkey (Callithrix jacchus): an anterograde and retrograde tract-tracing study. *J Comp Neurol*. **502**, 86–112 (2007).
45. D. H. Reser, K. J. Burman, H.-H. Yu, T. A. Chaplin, K. E. Richardson, K. H. Worthy, M. G. P. Rosa, Contrasting patterns of cortical input to architectural subdivisions of the area 8 complex: a retrograde tracing study in marmoset monkeys. *Cereb Cortex*. **23**, 1901–1922 (2013).
46. K. J. Burman, D. H. Reser, H.-H. Yu, M. G. P. Rosa, Cortical input to the frontal pole of the marmoset monkey. *Cereb Cortex*. **21**, 1712–1737 (2011).
47. L. Alexander, P. L. R. Gaskin, S. J. Sawiak, T. D. Fryer, Y. T. Hong, G. J. Cockcroft, H. F. Clarke, A. C. Roberts, Fractionating Blunted Reward Processing Characteristic of

Anhedonia by Over-Activating Primate Subgenual Anterior Cingulate Cortex. *Neuron*. **101**, 307-320.e6 (2019).

48. J. Selvanayagam, K. D. Johnston, D. J. Schaeffer, L. K. Hayrynen, S. Everling, Functional Localization of the Frontal Eye Fields in the Common Marmoset Using Microstimulation. *J Neurosci*. **39**, 9197–9206 (2019).
49. G. E. Eldred, G. V. Miller, W. S. Stark, L. Feeney-Burns, Lipofuscin: resolution of discrepant fluorescence data. *Science*. **216**, 757–759 (1982).
50. H. Skibbe, A. Watakabe, K. Nakae, C. E. Gutierrez, H. Tsukada, J. Hata, T. Kawase, R. Gong, A. Woodward, K. Doya, H. Okano, T. Yamamori, S. Ishii, MarmoNet: a pipeline for automated projection mapping of the common marmoset brain from whole-brain serial two-photon tomography. *arXiv:1908.00876 [cs, eess, q-bio, stat]* (2019) (available at http://arxiv.org/abs/1908.00876).
51. A. Woodward, R. Gong, H. Abe, K. Nakae, J. Hata, H. Skibbe, Y. Yamaguchi, S. Ishii, H. Okano, T. Yamamori, N. Ichinohe, The NanoZoomer artificial intelligence connectomics pipeline for tracer injection studies of the marmoset brain. *Brain Struct Funct*. **225**, 1225–1243 (2020).
52. A. Iriki, H. Okano,J., E. Sasaki, H. Okano, Eds., *The 3-dimensional atlas of the marmoset brain* (Springer Berlin Heidelberg, New York, NY, 2018), *Brain science*.
53. A. Woodward, T. Hashikawa, M. Maeda, T. Kaneko, K. Hikishima, A. Iriki, H. Okano, Y. Yamaguchi, The Brain/MINDS 3D digital marmoset brain atlas. *Sci Data*. **5**, 180009 (2018).
54. Y. Wan, H. Otsuna, H. A. Holman, B. Bagley, M. Ito, A. K. Lewis, M. Colasanto, G. Kardon, K. Ito, C. Hansen, FluoRender: joint freehand segmentation and visualization for many-channel fluorescence data analysis. *BMC Bioinformatics*. **18**, 280 (2017).
55. Natan, Fast 2D peak finder (https://www.mathworks.com/matlabcentral/fileexchange/37388-fast-2d-peak-finder), MATLAB Central File Exchange. Retrieved May 26, 2021. (2021).
56. N. Weed, T. Bakken, N. Graddis, N. Gouwens, D. Millman, M. Hawrylycz, J. Waters, Identification of genetic markers for cortical areas using a Random Forest classification routine and the Allen Mouse Brain Atlas. *PLoS One*. **14**, e0212898 (2019).
57. A. Sotiras, S. M. Resnick, C. Davatzikos, Finding imaging patterns of structural covariance via Non-Negative Matrix Factorization. *Neuroimage*. **108**, 1–16 (2015).
58. D. D. Lee, H. S. Seung, Learning the parts of objects by non-negative matrix factorization.

Nature. **401**, 788–791 (1999).

59. R. M. Braga, R. L. Buckner, Parallel Interdigitated Distributed Networks within the Individual Estimated by Intrinsic Functional Connectivity. *Neuron*. **95**, 457-471.e5 (2017).

60. T. Li, Q. Wang, J. Zhang, E. T. Rolls, W. Yang, L. Palaniyappan, L. Zhang, W. Cheng, Y. Yao, Z. Liu, X. Gong, Q. Luo, Y. Tang, T. J. Crow, M. R. Broome, K. Xu, C. Li, J. Wang, Z. Liu, G. Lu, F. Wang, J. Feng, Brain-Wide Analysis of Functional Connectivity in First-Episode and Chronic Stages of Schizophrenia. *Schizophr Bull*. **43**, 436–448 (2017).

61. G. Northoff, N. W. Duncan, How do abnormalities in the brain's spontaneous activity translate into symptoms in schizophrenia? From an overview of resting state activity findings to a proposed spatiotemporal psychopathology. *Prog Neurobiol*. **145–146**, 26–45 (2016).

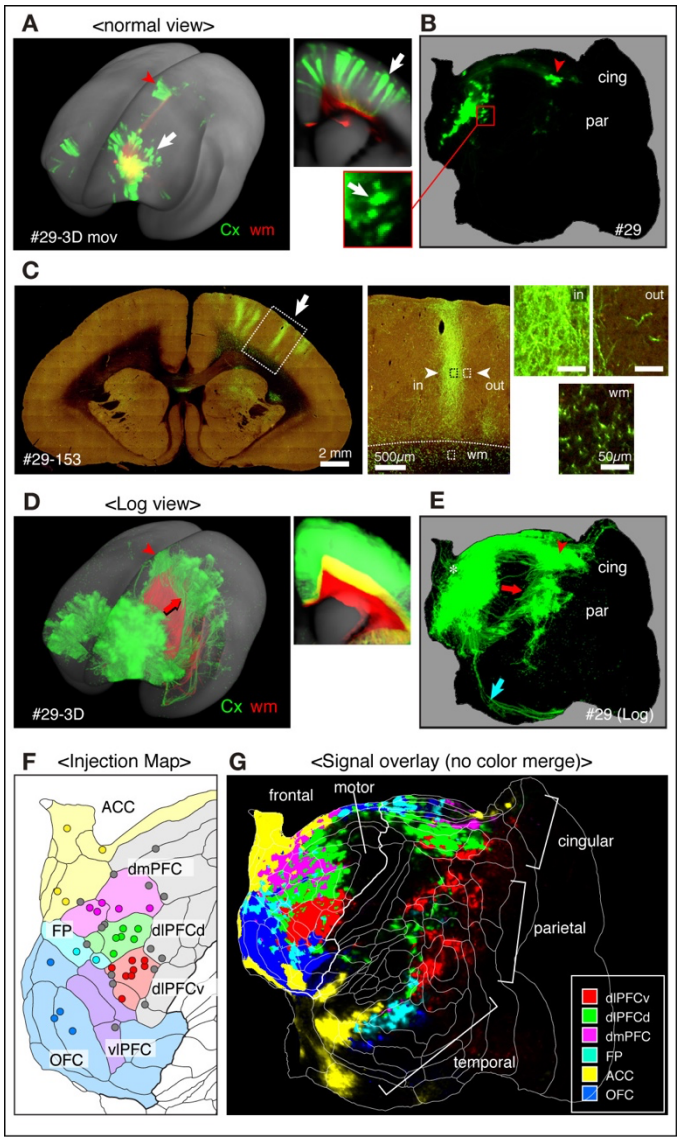

Fig. 1: Prefrontal cortex (PFC) projections exhibit highly focal patterns immersed in sparse but widespread patterns. (A) Three-dimensional (3D) reconstruction of the tracer signals in the standard coordinate. The cortical (Cx) and white matter (wm) signals are colored in green and red, respectively. The white arrows indicate the same columnar projections shown in the other panels. **(B)** MIP view of the flatmap stack (Fig. S1E for 3D view). cing, cingular field; par, parietal field. See Fig. S2 for area annotation. **(C)** Original section image at different magnifications. wm; white matter. **(D)** Visualization of weak signals by lowering the threshold and log-transformation. Same data as shown in panel (A). The red arrow symbolizes the axonal projections in the white matter, which are beneath the flatmap stack in panel (E) (also see Fig. S1H and S1I). **(E)** Log-transformed version of flatmap stack data. Detection of weak and sparse signals toward the parahippocampal region is highlighted by the cyan arrow (also see Fig. S1F). **(F)** Summary of injections analyzed in this study (also see Fig. S1J). The colored dots represent the core PFC injections analyzed in this study. **(G)** Overlay of projections by winner-take-all style (no color merge). Also, see Fig. S1K.

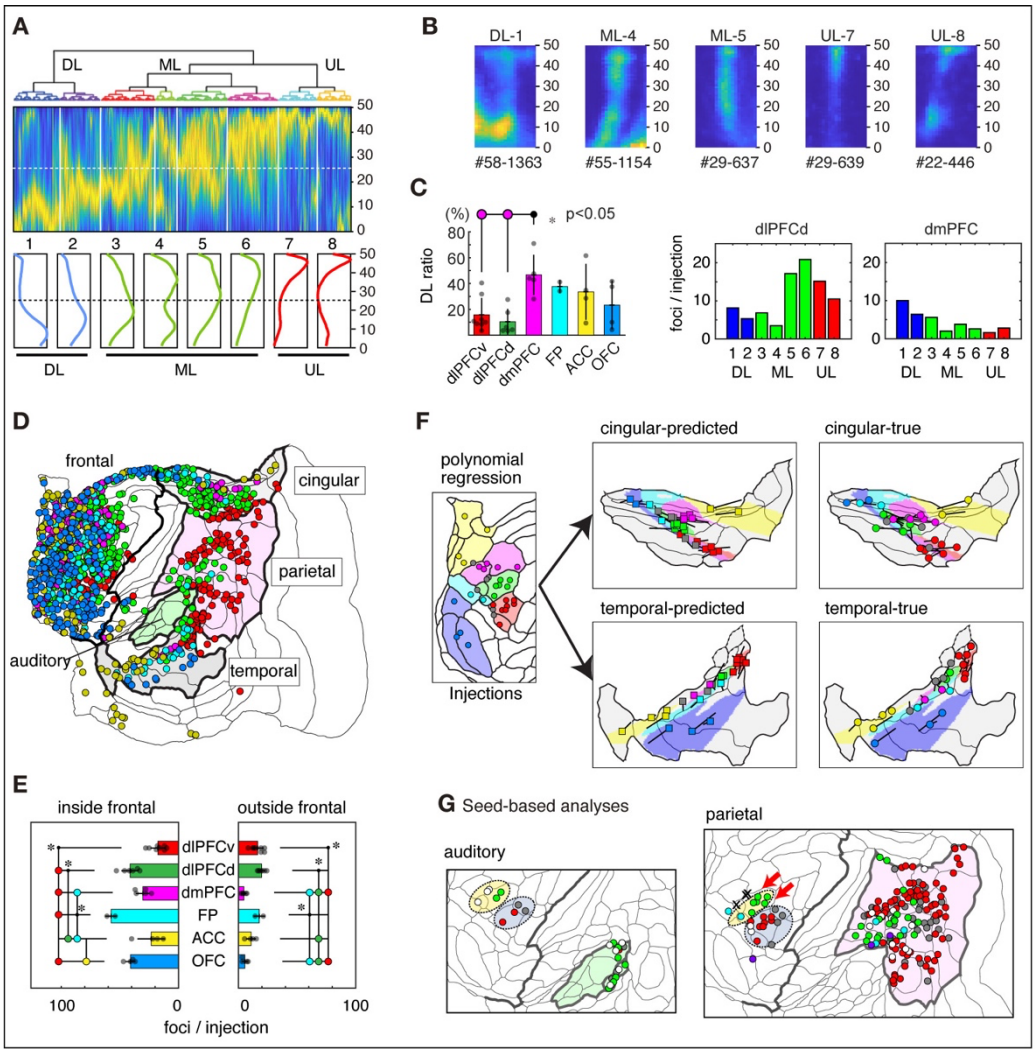

Fig. 2: Laminar and areal analyses of 'focal' corticocortical projections. (A) Lamina profiles for the 1867 tracer foci. The averaged profiles of eight clusters are shown below. **(B)** Representative laminar patterns of tracer foci. **(C)** The ratios of DL types among the tracer foci shown for six PFC subregions. The colored circles indicate statistically significant differences (ANOVA with Tukey's honest significant difference test, $p<0.05$) between the subregions of those colors and the subregions beneath the circles. Averaged distribution patterns for dlPFCd and dmPFC are shown as examples. See Fig. S3F. **(D)** Cortical areal distribution of tracer foci for the six PFC subregions in four association area fields. **(E)** The average numbers of tracer foci per injection for six PFC subregions. **(F)** Prediction of topographic projections toward the cingular and temporal fields based on the injection coordinates (see Fig. S5). The line bars indicate deviation of predicted and the true positions. **(G)** Seed-based analyses to determine injections that exhibited focal projection within the target fields. The colors of the injection and tracer foci indicate which subregion they belong to (FP, cyan; dlPFCd, green; dlPFCv, red; PM, grey; white, border). The red arrows indicate borders of abrupt changes in projection profiles.

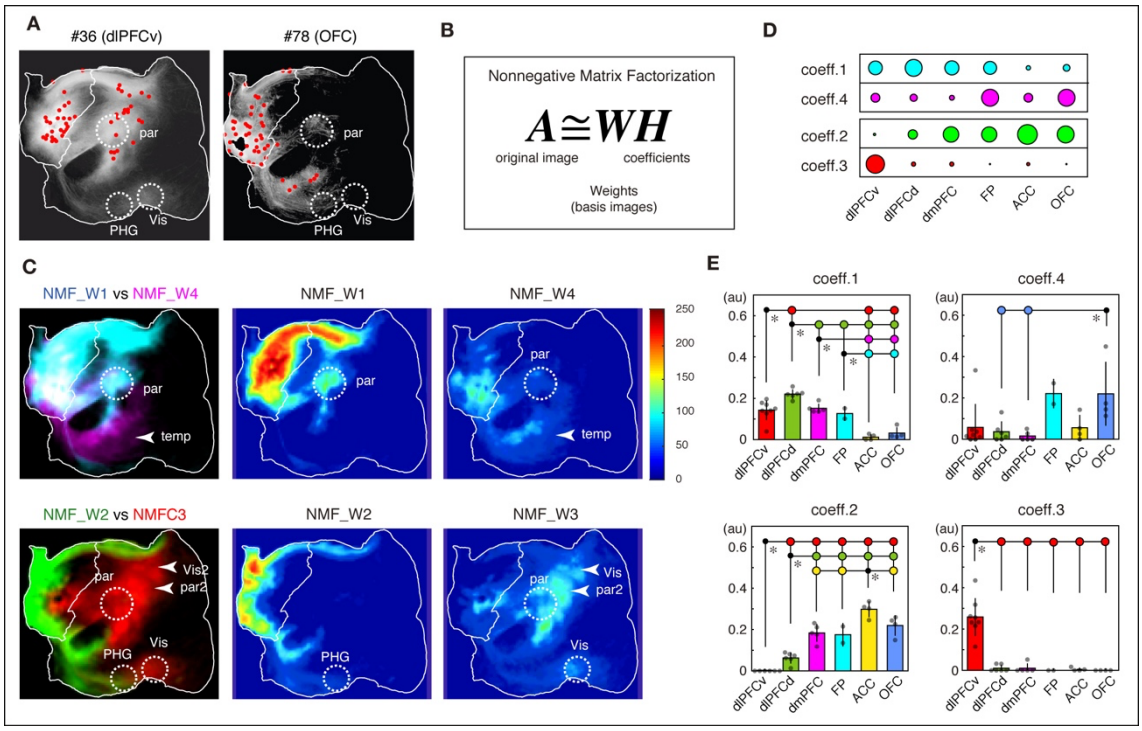

Fig. 3: Characterization of widespread corticocortical projections in logscale view by nonnegative matrix factorization (NMF) analysis. (A) Log-transformed tracer images for two examples (see Fig. S6A for more examples). The red dots indicate the tracer foci of the same samples. Note the presence of weak signals in dotted circles, where there may not exist any tracer foci. par, parietal area; PHG, perihippocampal gyrus; Vis, visual area. **(B)** Decomposition of the original image into weights (basis images) and coefficients by NMF. **(C)** Four components obtained by the NMF analyses in two pairs. The dotted circles and arrowheads highlight regions with characteristic projections. **(D)** Contribution of four components to the prefrontal cortex (PFC) subregion patterns. The areas of circles indicate averaged values for coeff. 1–4 for six PFC subregions shown in panel (E). **(E)** Coefficients of different PFC subregions. See the legend for Fig. 2C for statistical significance.

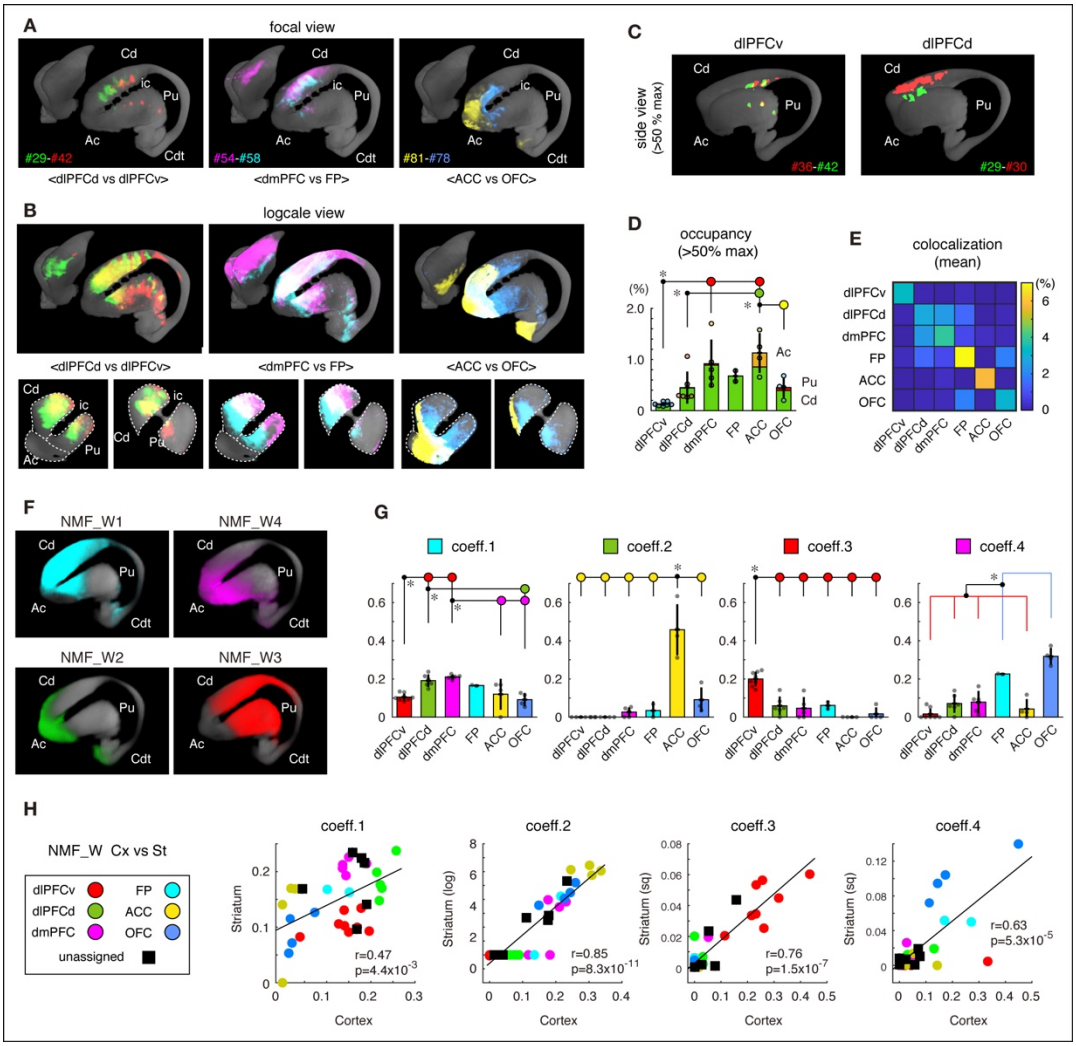

Fig. 4: Characterization of focal and spread corticostriatal projections. **(A)** The bilateral three-dimensional (3D) representation of focal and diffuse striatal projections for exemplary cases. See Supplementary Movie 3 for rotation views. Ac, nucleus accumbens; Cd, caudate nucleus; Cdt, tail of the caudate nucleus; Pu, putamen; ic, internal capsule. **(B)** The logscale view of the same data show diffuse spread of the tracer signals. Lower panels show coronal section views at two AP positions. **(C)** Interdigitation of focal projections visualized by binarization at 50% of the maximum values. **(D)** Occupancies of the binarized signals in the striatal volume. The averaged occupancies in the caudate, putamen, and nucleus accumbens are overlaid. **(E)** Averaged co-localization within and across subregions. Also, see Fig. S7C. **(F)** NMF_W1-4 in 3D representation. See Fig. S7H for overlay. **(G)** Coefficients of different subregions for each component. **(H)** Similarity of coeff. 1–4 between cortical and striatal projections shown by scatter plots. Spearman's rank correlations and p-values are shown for each panel. The scatter plots employed either the original value (for coeff. 1) or log-transformed (for coeff. 2) or squared values (for coeff. 3 and 4).

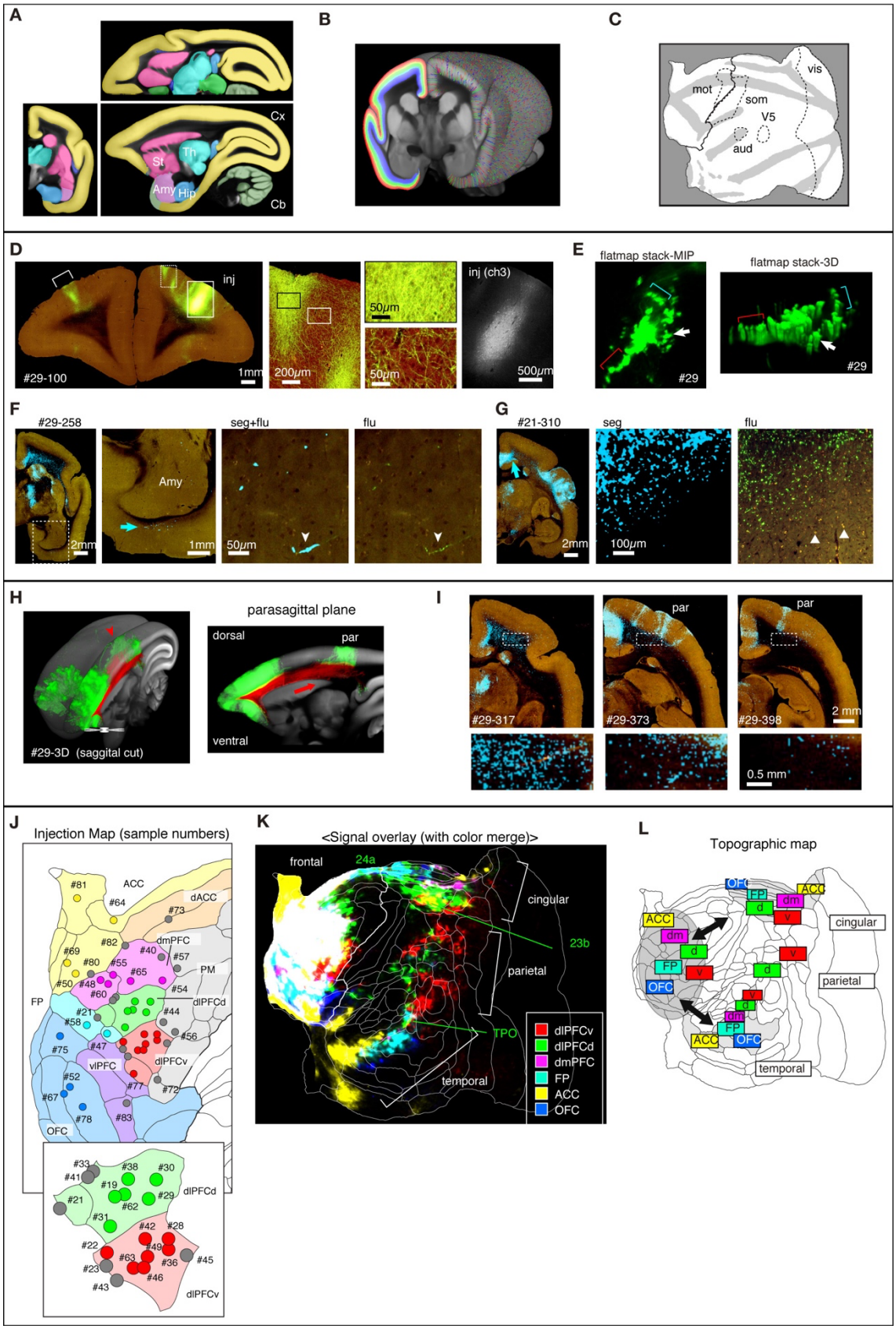
A
Cx
St
Th
Amy
Hip
Cb
B
C
vis
mot
som
V5
aud
D
inj
#29-100
1mm
200μm
50μm
50μm
inj (ch3)
500μm
E
flatmap stack-MIP
flatmap stack-3D
#29
#29
F
#29-258
seg+flu
flu
Amy
2mm
1mm
50μm
G
#21-310
seg
flu
2mm
100μm
H
parasagittal plane
dorsal
par
ventral
#29-3D (saggital cut)
I
par
par
#29-317
#29-373
#29-398
2 mm
0.5 mm
J
Injection Map (sample numbers)
ACC
dACC
dmPFC
PM
FP
dlPFCd
vlPFC
dlPFCv
OFC
K
<Signal overlay (with color merge)>
frontal
24a
cingular
23b
parietal
TPO
temporal
dlPFCv
dlPFCd
dmPFC
FP
ACC
OFC
L
Topographic map
cingular
parietal
temporal

910

911

Fig. S1: Projection tracing by serial two-photon tomography imaging (STPT). (A) The section views for the STPT template overlaid with anatomical annotations. Cx, cortex; St, striatum; Th, thalamus; Amy, amygdala; Hip, hippocampus; Cb, cerebellum. **(B)** Schematic representation of the vertices that determined the columnar structures of the cortical surface (right side) and the lamina structures determined by these vertices (left side). This information was used to convert the cortical surface into a stack of 50 layer-specific flatmaps. **(C)** Schematic representation of the areal structure and distortion of the flatmap stack. Dotted lines indicate the positions of primary areas, including visual area V1 (vis), auditory area AuA1 (aud), somatosensory areas (som) A3a, A3b, and A1/2 and motor areas (mot) A4ab, A4c, and A24d. Frontal areas, including the PFC, premotor and motor areas, are positioned to the left of the solid line. The gray regions correspond to the ridge regions in 3D, which showed shrinkage (<0.7) at the bottom layer upon flatmapping. **(D)** Example section image (section 100 of sample #29) near the injection site. The boxed regions are magnified in the right-hand panels. Note the high concentration of axonal signals in the "columnar" region (boxed black) compared with the outside (boxed white). Although the fluorescence near the injection site (inj) is saturated in the red (Ch1) and green (Ch2) channels (data not shown), the fluorescence in the blue (Ch3) channel showed unsaturated cell body signals and was used to identify the cells of origin of the projections. The bracket in the left panel indicates the contralateral columnar projection represented by a 3D movie in Supplementary Movie 2. **(E)** Magnified view of the flatmap stack surrounding the injection site; the white arrow indicates the column shown in Fig. 1A. The green bracket shows the columnar projections, part of which is shown in Fig. S1D. **(F)** The original section images containing weak axon signals corresponding to the cyan arrow in Fig. 1E. Fluorescence images are overlaid with cyan-colored segmentation. The white arrowhead shows bouton-like varicosities. **(G)** Comparison of tracer segmentation (seg; cyan) and original fluorescence (flu). Aged marmoset brains typically have many dot-like autofluorescences of lipofuscin(*49*) (shown by white arrowheads), which are distinguishable by the ch1/ch2 ratio. **(H)** Parasagittal dissection of the 3D views in Fig. 1D demonstrates the segregation of the connecting fibers in the white matter (red) from the cortical signals (green). par, the parietal region indicated in Fig. S1I. **(I)** The spread of axon signals in the white matter and convergence of multiple columnar foci in the parietal (par) region. The segmented tracer signals are shown in cyan and overlaid onto the original fluorescence images. **(J)** Positions of injections for six PFC subregions (dlPFCd, green; dlPFCv, red; dmPFC, magenta; FP, cyan; ACC, yellow; OFC, blue) and others (gray). These colored injections were used as core samples for various analyses. Depending on the analyses, gray injections that were placed outside the six PFC subregions (e.g., premotor areas) or placed on the borders between subregions were also used. See Table S1. **(K)** The overlay of projection patterns for six PFC subregions that allows color mixing. The convergence of projections from different subregions in A24a, A23b, and TPO, as well as most frontal areas, resulted in color mixing. Same as in Fig. 1G, except for color mixing. **(L)**A schematic representation of the topographic projections deduced from the overlay of tracer signals for the six PFC subregions shown in Fig. 1G. d; dlPFCd, v;dlPFCv, dm; dmPFC.

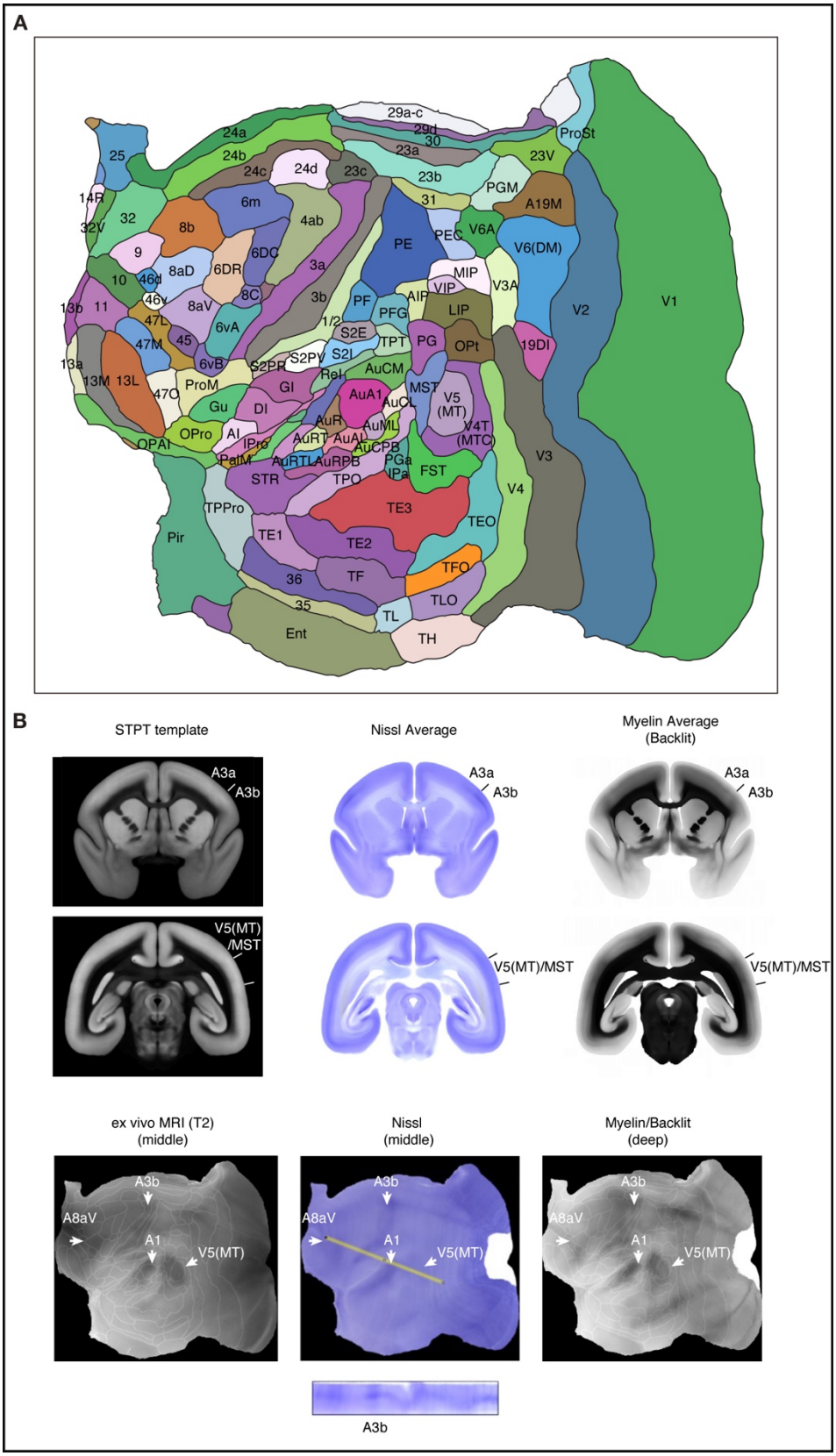
A
29a-c
29d
30
ProSt
24a
24b
24c
24d
23c
23a
23V
25
23b
PGM
14R
6m
31
A19M
32V
32
8b
4ab
PEC
V6A
V6(DM)
9
6DC
PE
MIP
10
46d
8aD
6DR
3a
VIP
V3A
46v
8C
3b
PF
AIP
V2
V1
13b
11
8aV
PFG
LIP
47L
6vA
1/2
S2E
47M
45
TPT
PG
OPt
19DI
13a
6vB
S2PR
S2PV
S2I
AuCM
13M
13L
ProM
GI
ReI
MST
47O
AuA1
V5
(MT)
Gu
DI
AuCL
AuR
AuML
V4T
(MTC)
OPro
AI
AuRT
AuAL
OPAI
IPro
AuCPB
PaIM
AuRTL
AuRPB
PGa
IPa
FST
V3
STR
TPO
V4
TPPro
TE3
TEO
Pir
TE1
TE2
TFO
36
TF
TLO
35
TL
Ent
TH
B
STPT template
Nissl Average
Myelin Average
(Backlit)
A3a
A3b
V5(MT)
/MST
V5(MT)/MST
ex vivo MRI (T2)
(middle)
Nissl
(middle)
Myelin/Backlit
(deep)
A8aV
A1
V5(MT)
A3b

Fig. S2: A map of the cortical areas and comparison with histological data. (A) The cortical area annotation of the Brain/MINDS atlas(*51*, *52*) is transferred to the standard reference space (STPT template) and the flatmap stack for registration. **(B)** Comparison of the cortical annotation of the STPT template with histological data. After STPT imaging, one in ten sections were retrieved for Nissl staining and backlit myelin imaging (see Methods). Here, the section views and flatmap views for the averaged images of Nissl and backlit myelin imaging are shown. Several conspicuous landmarks in these images corresponded well to cortical annotations.

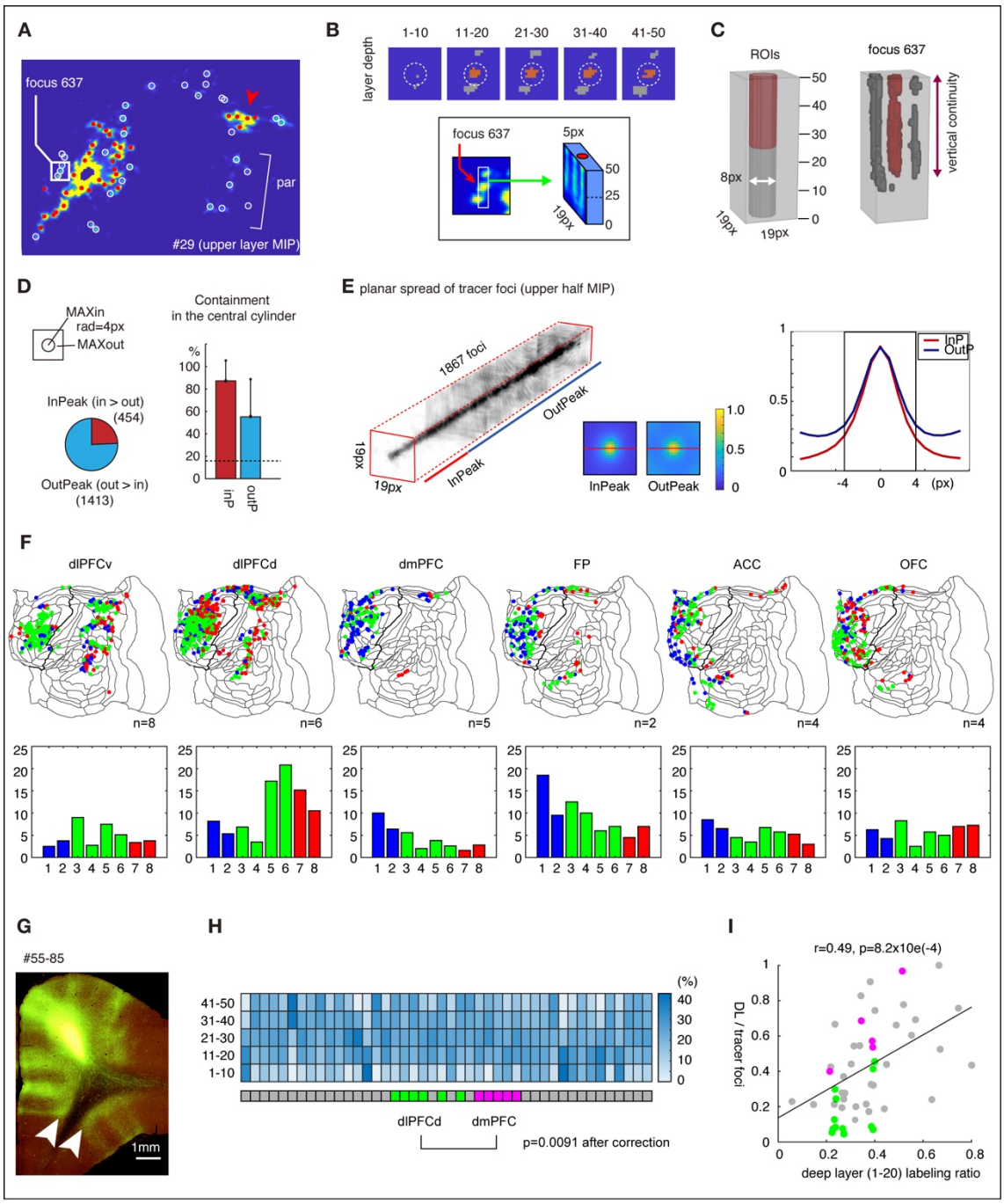
A
focus 637
par
#29 (upper layer MIP)
B
layer depth
1-10
11-20
21-30
31-40
41-50
focus 637
5px
19px
C
ROIs
focus 637
8px
19px
19px
vertical continuity
D
MAXin
rad=4px
MAXout
Containment
in the central cylinder
InPeak (in > out)
(454)
OutPeak (out > in)
(1413)
inP
outP
E planar spread of tracer foci (upper half MIP)
1867 foci
19px
19px
InPeak
OutPeak
InPeak
OutPeak
InP
OutP
(px)
F
dlPFCv
dlPFCd
dmPFC
FP
ACC
OFC
n=8
n=6
n=5
n=2
n=4
n=4
G
#55-85
1mm
H
41-50
31-40
21-30
11-20
1-10
(%)
dlPFCd
dmPFC
p=0.0091 after correction
I
r=0.49, p=8.2x10e(-4)
DL / tracer foci
deep layer (1-20) labeling ratio

968

969

Fig. S3: Laminar and areal analyses of focal corticocortical projections. (A) Detection of tracer foci in the cortical flatmap stack. The average of the upper layers of the flatmap stack (26–50) was used to detect the tracer foci as local maxima. Red and white circles indicate foci with peak values that are >1/10 and >1/100 of the standardization value (see Methods for details), respectively. The red arrowhead indicates the clusters of cingular tracer foci shown in Fig. 1A and 1B. par, parietal field. **(B)** Layer-specific view of focus 637 with surrounding foci showing vertical continuity. The dotted circle indicates the central cylinder with a 4-pixel radius. The tracer signals are thresholded at half the maximum value within the upper part of the central cylinder for binarization, and the continuous clump is selected for red coloring. The 3D view of the focus 637 and the adjacent foci before binarization are shown boxed below. **(C)** 3D reconstruction of binarized tracer signals. The right panel shows an example of a binary clump that is consecutive to the largest clump in the center of the foci (red region in the left panel). Vertical continuity is measured as the height of these clumps, which were 21 ± 13 and 32 ± 16 pixels, respectively, for the InP and OutP groups (see below). **(D)** Analysis of signal convergence to the central cylinder. The tracer foci were classified into InPeak (InP) and OutPeak (OutP) groups, based on whether the maximum value within the upper cylinder ROI (MAXin) is higher or lower than the outside maximum (MAXout). The abundance of these groups is shown in the pi plot. Signal convergence is measured by the percentage of positive voxels within the central cylinder to the total number of positive voxels within the 19 × 19 × 50 cuboid. The dotted line indicates the expected value of the random distribution calculated from the voxel sizes of the ROIs. Error bar: standard deviation (SD). **(E)** The 19 × 19 pixel planar spread for 1867 tracer foci are aligned in 3D to show the central convergence of the tracer signals. The InPeak and OutPeak groups defined in panel (D) are shown separately. The averaged images and averaged tracer intensities along the red sampling line for these two groups are plotted as indicated. **(F)** Areal distribution of three lamina types (DL: blue, ML: green, UL: red) for each PFC subregion and the bar graphs of tracer foci classified into eight clusters. The colors of the bar graphs indicate the DL, ML, and UL types. The areal distribution shows the overlay of all samples, and the bar graphs show the average values per injection. **(G)** An example image shows widespread innervation in layer 6 (arrowheads) for dmPFC injection. **(H)** Lamina distribution of cell body labeling at injection sites. The color bar below the heatmap indicates the subregions of interest shown in panel (I). The p-value of the differential DL ratio after correction is shown. **(I)** Correlation between the ratio of DL types among tracer foci against the ratio of deep layer (1–20) labeling. The injection depth appears to have a weak effect on the lamina profiles of the tracer foci ($r = 0.49$, $p = 8.0 \times 10e\text{-}4$), consistent with a macaque report(*15*). However, the ratio of DL types between the tracer foci for the dmPFC (magenta) and dlPFCd (green) showed deviations even after correction for such an effect.

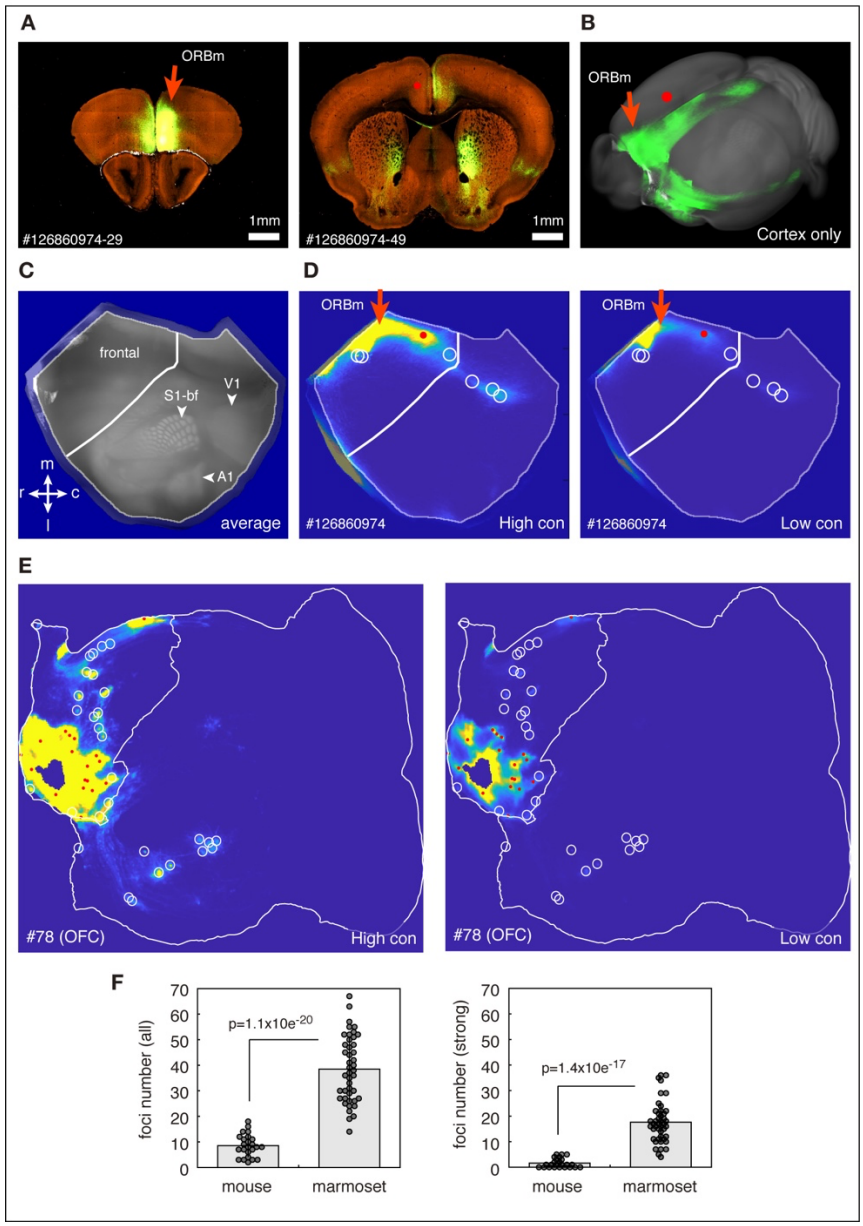

Fig. S4: Comparison of mouse and marmoset data for focal projections. (A) Section images of a tracer experiment with an injection into ORBm (126860974) retrieved from Mouse Brain Connectivity Atlas (*5*, *6*). **(B)** 3D reconstructed image of the cortical projection data. **(C)** The flatmap image for the averaged background fluorescence for cortical landmarks. Considering the distortion, the fringes of the flatmap were excluded from foci detection. The white line in the middle indicates the border between the motor and somatosensory areas. S1-bf; S1 barrel field. **(D)** Flatmap images of the ORBm injection at high and low contrasts to show both strong and weak signals. Red dots and white circles indicate foci with peak values that are >1/10 and >1/100 of the standardization value (see Methods for details), respectively. **(E)** Detection of tracer foci for #78 (OFC) using the mean of all layers for comparison with the mouse data. **(F)** Comparison of detected tracer foci between mouse and marmoset. The right panel compared only the strong signals (those shown by red dots). See Table S2 for the information on the mouse data used in this analysis. All 44 samples were used for the marmoset data. For this comparison, we performed a new foci detection search using the flatmaps of all layers instead of upper layer flatmaps.

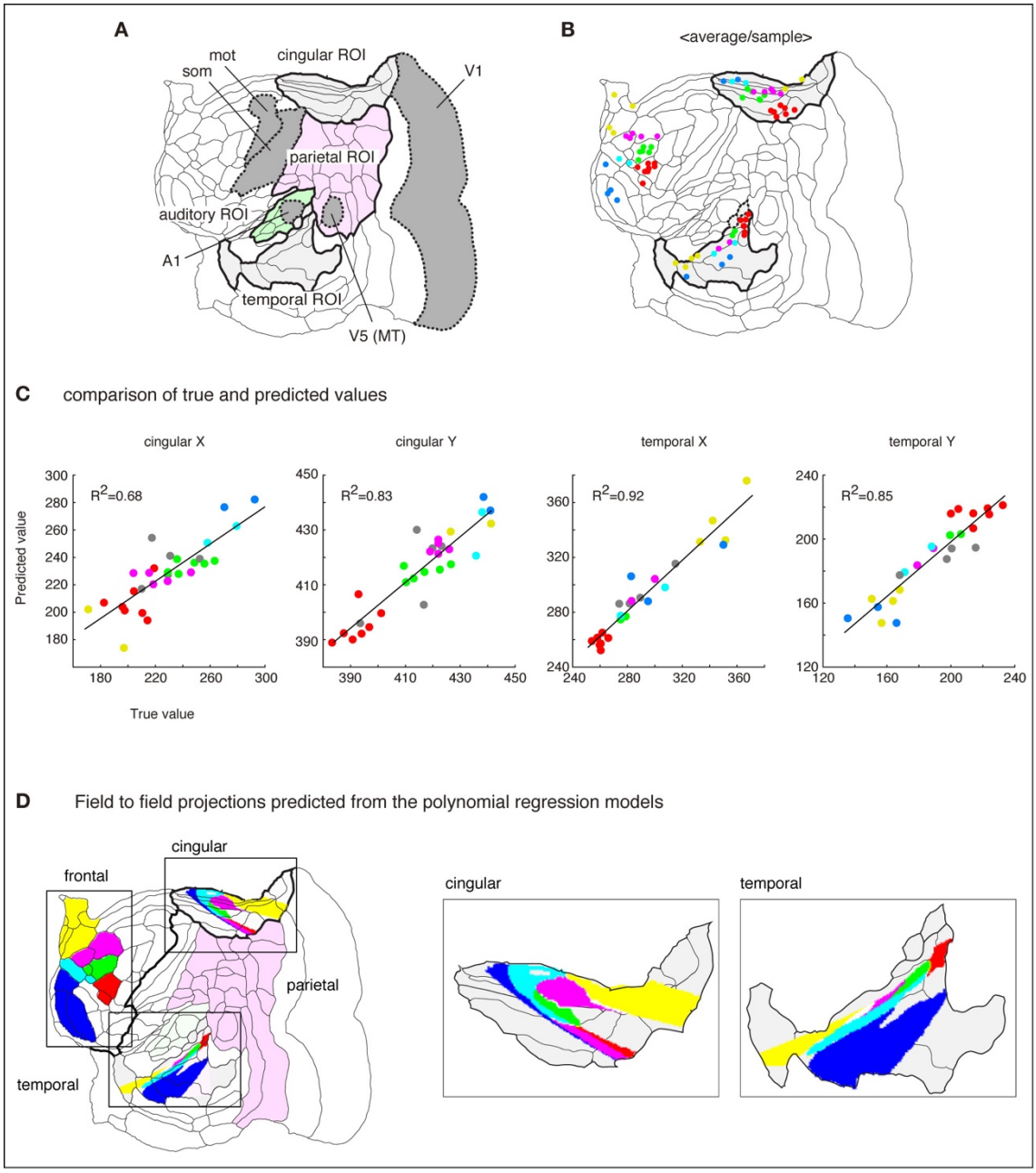

Fig. S5: Polynomial regression fitting for focal projections toward the cingular and temporal fields. **(A)** ROIs to classify the positions of tracer foci into the cingular, temporal, parietal association area fields, and auditory area fields (core and belt). Belt areas (AuML and AuCL) are included in both the auditory and temporal field areas. The primary areas and V5 are shown by gray shading (see Fig. S1C for annotations). **(B)**The averaged positions of the tracer foci for each injection are determined separately for the cingular and temporal fields. Each dot represents the average position of the tracer foci for one injection. **(C)** Comparison of true and predicted values from polynomial regression models. The colored dots represent the injections into six PFC subregions, and the gray dots represent the border injections. Injections into the caudal PM, dACC, and vlPFC are excluded from the calculations. **(D)** Every point in the PFC area is subjected to polynomial models to predict field-to-field projections. The same data are used for Fig. 2E.

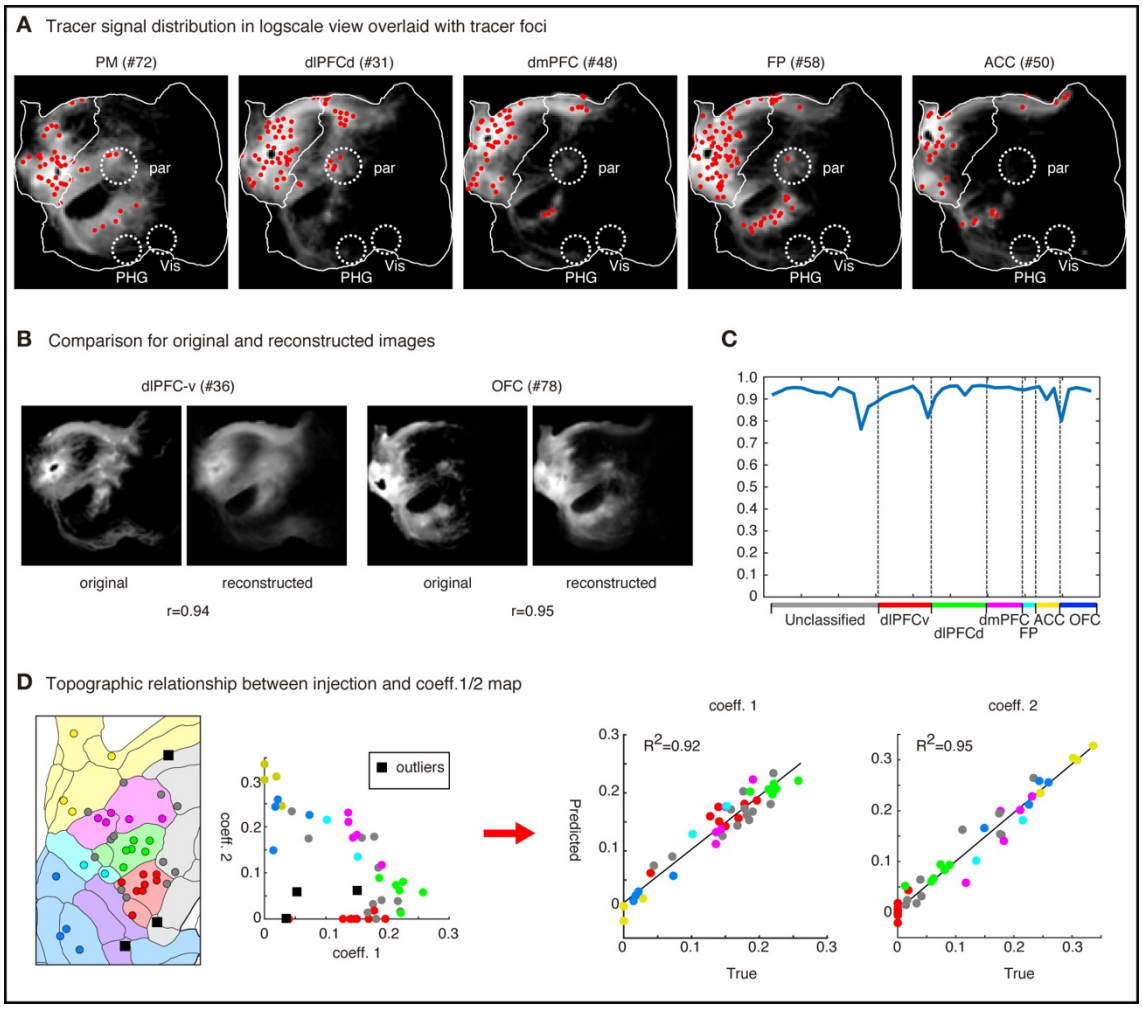

Fig. S6: Characterization of widespread corticocortical projections in logscale view. (A) Log-transformed tracer images representing various frontal subregions, including premotor areas (PM), with tracer foci overlaid (red dots). **(B)** Comparison of original images and those reconstructed from the four NMF components. **(C)** The accuracy of the reconstruction is measured using the correlation coefficients of the two images for 44 pairs. **(D)** Comparison of topographic relationships of injection sites with plot positions in the coeff. 1/2 value map. We observed similarities between them, except for three outliers positioned at the caudal end (black squares). The polynomial regression models could predict these coefficients based on injection coordinates as shown.

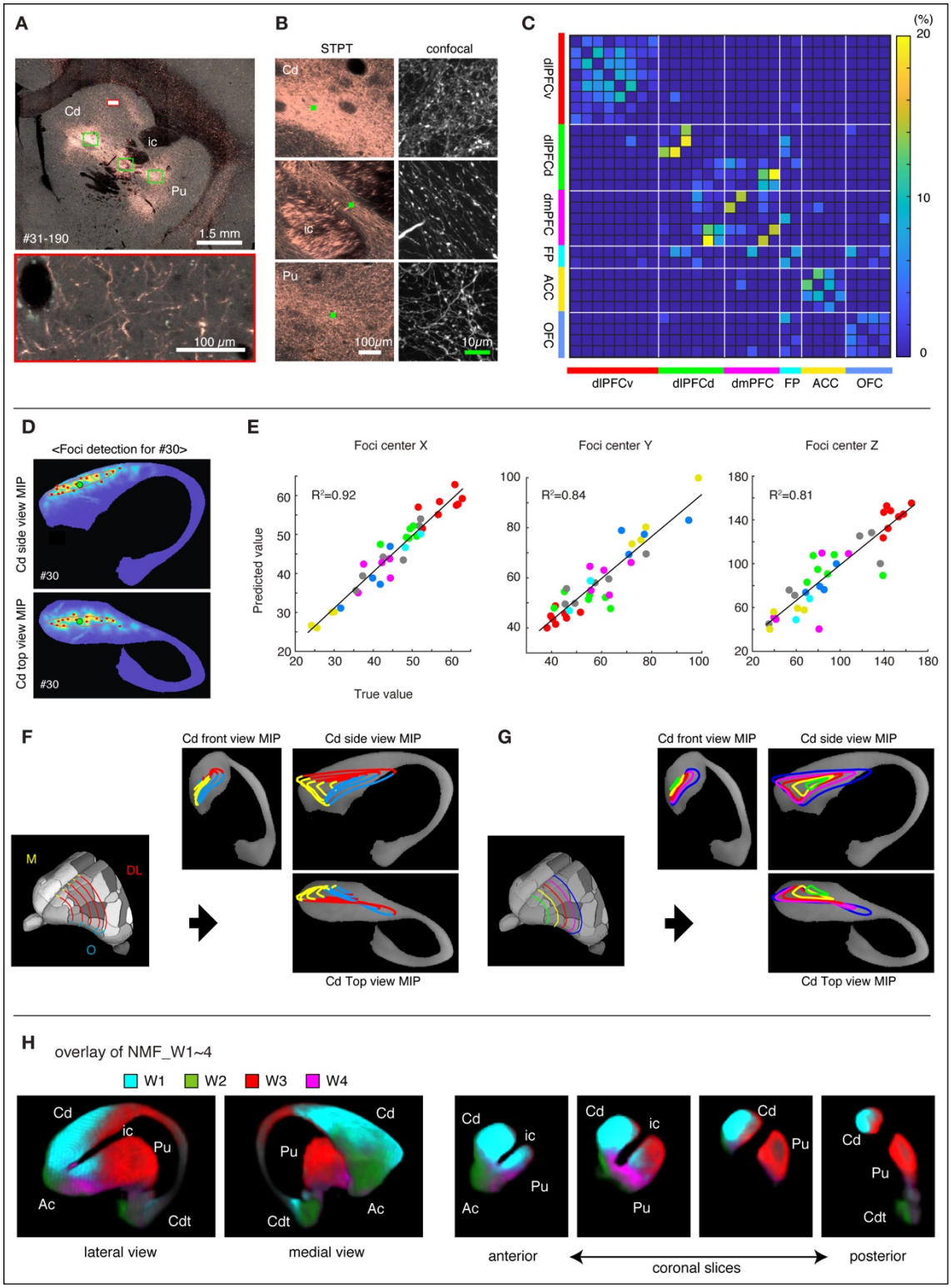
A
Cd
ic
Pu
#31-190
1.5 mm
100 μm
B
STPT
confocal
Cd
ic
Pu
100μm
10μm
C
(%)
20
10
0
dlPFCv
dlPFCd
dmPFC
FP
ACC
OFC
D
<Foci detection for #30>
Cd side view MIP
Cd top view MIP
#30
E
Foci center X
Foci center Y
Foci center Z
R²=0.92
R²=0.84
R²=0.81
Predicted value
True value
F
Cd front view MIP
Cd side view MIP
Cd Top view MIP
M
DL
O
G
Cd front view MIP
Cd side view MIP
Cd Top view MIP
H
overlay of NMF_W1~4
W1
W2
W3
W4
Cd
ic
Pu
Ac
Cdt
lateral view
medial view
anterior
coronal slices
posterior

1050
1051

Fig. S7: Focal and spread corticostriatal projections. (A) Example of the original section image of striatal projections. Here, the fluorescence of the tracer signals is colored pink. The white rectangle with red contours is magnified below as an example of a sparsely innervated region. The three green rectangles are magnified in the pane. **(B)** A clump of dense tracer signals in Cd, a bridge region in the internal capsule, and a dense region in Pu are shown magnified. The green-filled rectangles in the STPT images indicate the approximate positions for confocal microscopy on the right panels. **(C)** The colocalization of binarized tracer signals between two samples within and across six PFC subregions. See Fig. 4C for example images, and Fig. 4E for the averaged values. Note the large sample variance in the extent of colocalization. The average rate of colocalization was generally higher within the same PFC subregion than between different subregions (Fig. 4E), except that some dlPFCd samples showed similar distributions to dmPFC samples. Overall, however, the colocalization rate was low. **(D)** Detection of local maxima of tracer convergence foci; the average position of these foci is indicated by a black circle. The MIP side view and top view of the left caudate nucleus are shown. **(E)** Polynomial regression fitting to predict the striatal projection targets based on injection coordinates. Six core PFC subregions and border injections are used for regression fitting. **(F)** Topographic projections from the frontal areas to the caudate nucleus predicted by the polynomial regression model. Five contours covering the dorsolateral (DL; red), orbital (O; blue), and medial (M; yellow) sides of the frontal cortex are projected onto the caudate nucleus. **(G)** The five contours colored green, yellow, orange, red, and blue from the rostral to the caudal end are projected onto the caudate nucleus. **(H)** NMF components of the spread projections shown in Fig. 4F are overlaid to highlight the differential positions. The coronal sections roughly correspond to AP+12.5, AP+11.5, AP+9.0, and AP+7.0 in the Paxinos atlas(*37*) (https://www.marmosetbrain.org/reference). Ac, nucleus accumbens; Cd, caudate nucleus; Cdt, tail of caudate nucleus; Pu, putamen; ic, internal capsule.

Normal state

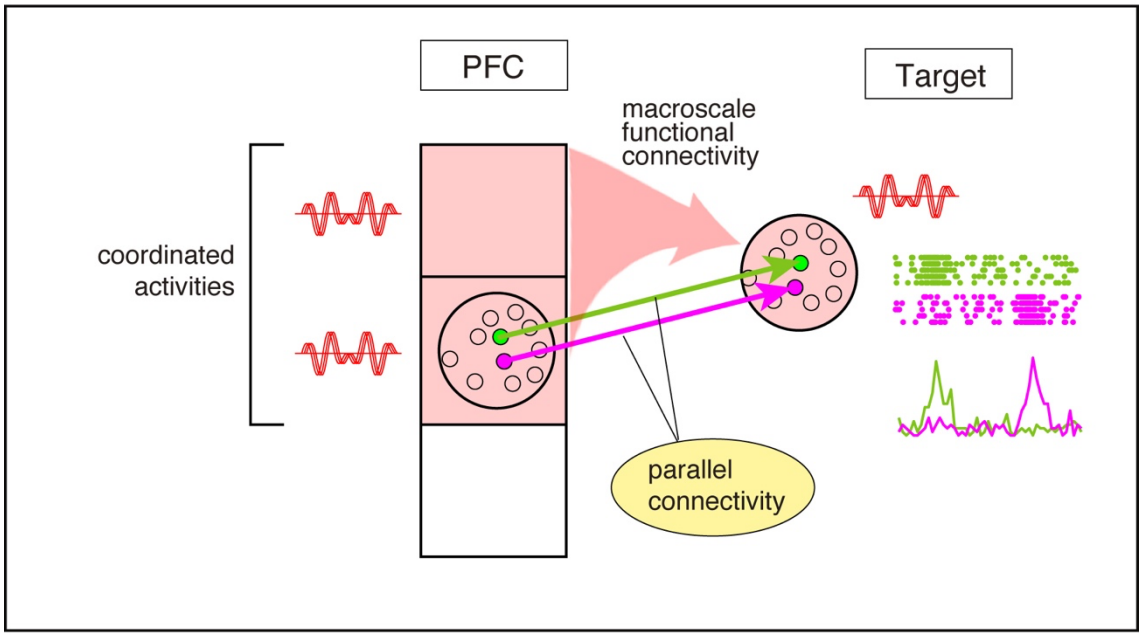

Disease state

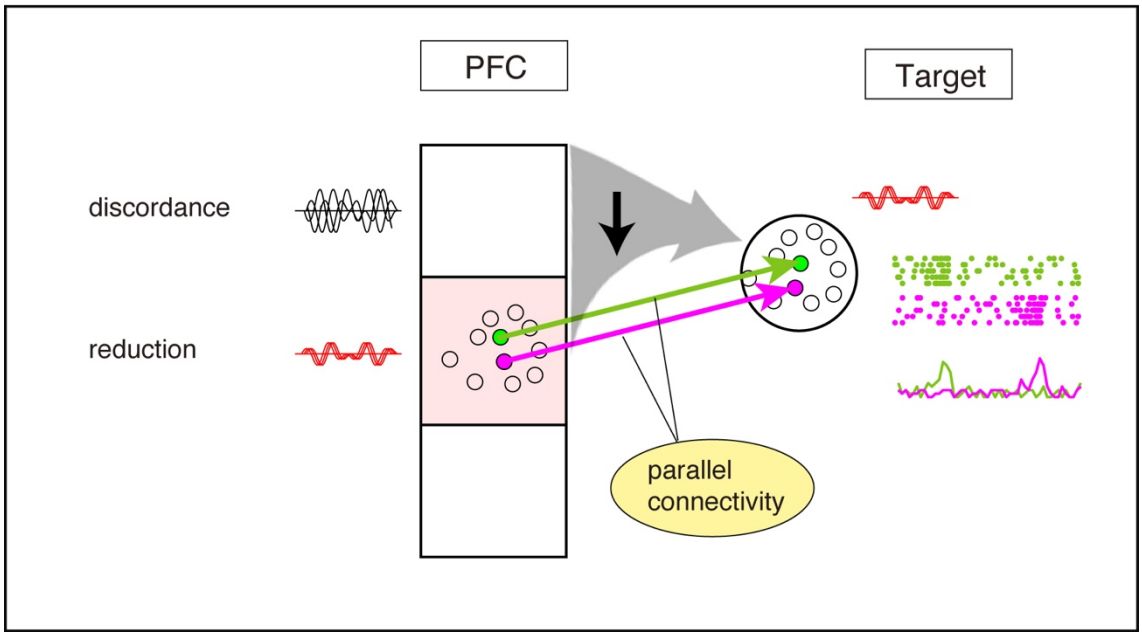

Fig. S8: A model for differential effects of focal and spread projections. [Normal state] A model explaining the state-dependent effects of focal and widespread projections. An important implication of this model is that structural connectivity can only define the framework of brain circuits. The manner in which the circuit works depends on the dynamic state of the entire system. In this panel, two focal-type projections are shown in green and magenta and one spread-type projection is shown by a large arrow (red). The focal-type projections originate from neuronal populations located within the submillimeter range and target narrow spots in the target brain regions (cortical or striatal tracer foci). Due to the high convergence of axon fibers in small areas, the activities of individual neurons in the source region are expected to be conveyed to the target region with high efficacy and little intermixing. Such connectivity should support distributed parallel processing of complex information [e.g., (*59*)]. Meanwhile, PFC neurons also have widespread projections with much lower densities. Due to similar projection preferences in nearby locations, neurons in a wide region exhibit extensive overlap in the target regions (shown by a large arrow). Unlike focal projections, the contributions of single neurons are spread out and not very strong. However, if many neurons exhibit coordinated activities, they should have significant impacts due to cumulative effects. This could be a neural substrate of macroscale functional connectivity. We hypothesize that such activity-dependent effects may have a modulatory effect on the neural transmission through the focal-type projections. [Disease state] Disease conditions (e.g., schizophrenia and Alzheimer's disease) are often associated with modification of functional connectivity networks(*28*, *60*, *61*). In this model, we can explain such modification to be caused by chronic reduction or discordance in the global PFC activity, which in turn may lead to the reduction or abortion of the modulatory effects on the focal connectivity.

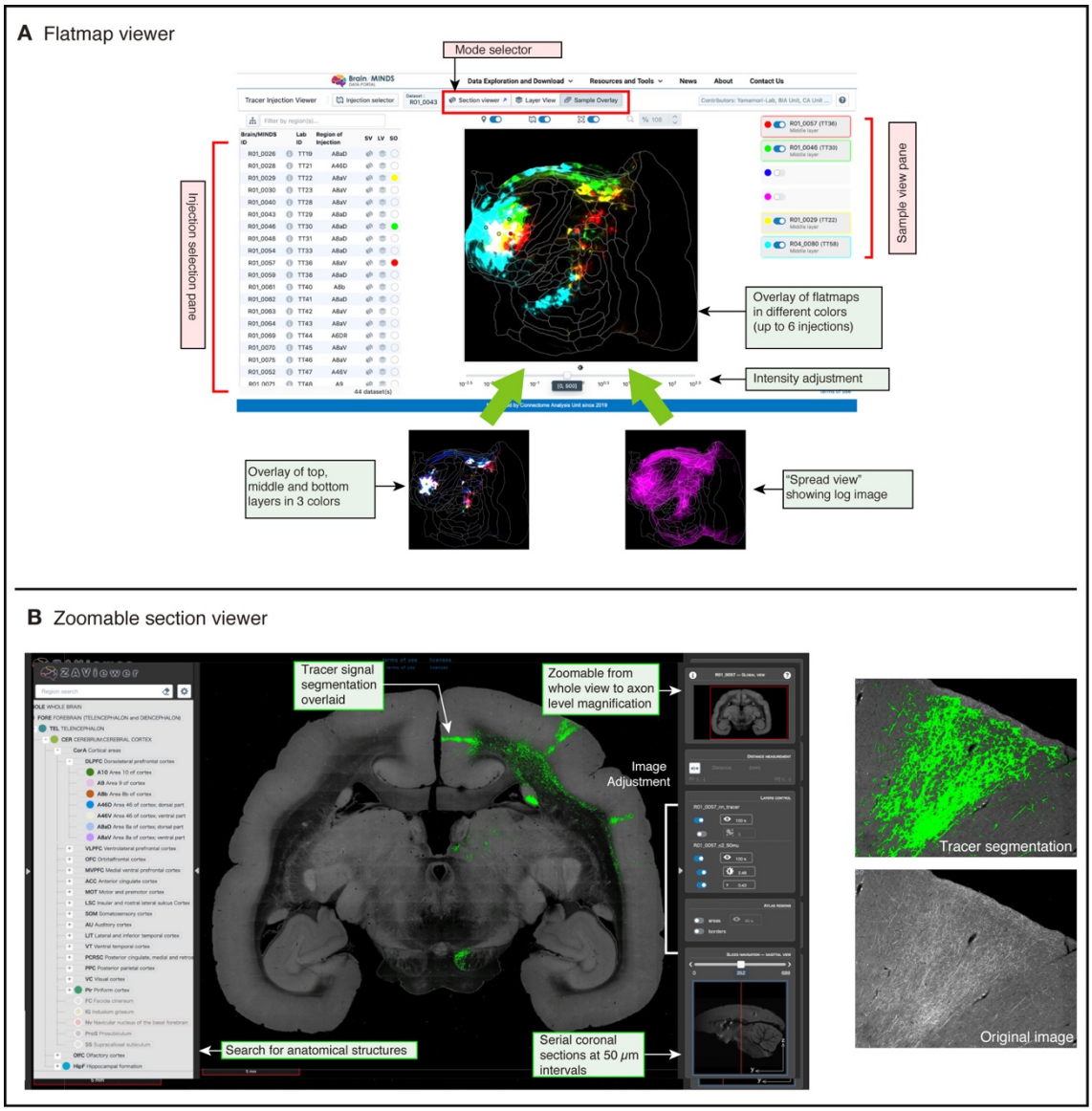

Fig. S9: Flatmap viewer and Zoomable section viewer for data visualization. (A) Flatmap viewer for visualization of flatmap stack data; there are three buttons for "Mode selector." "Section Viewer" opens the Zoomable section viewer. "Layer view" shows the layer structures of the selected sample in three colors or the spread view of log-transformed low threshold image (shown below). The sample overlay" shows the overlay of multiple samples with different colors (up to six samples). **(B)** Zoomable section viewer shows the original fluorescent image and tracer segmentation for all serial coronal sections of the entire brain. Segmented tracer signals are readily visible at low magnification and can be smoothly magnified to show axon-level details.

Data ID	Brain/MINDS ID	age (y)	sex	subregion	area	Core 6 PFC
#40	R01_0061	8.5	M	PM/dmPFC	A8b/A6DM	
#56	R01_0083	6	F	PM	A6DR	
#57	R04_0079	4.3	F	PM	A6DM	
#72	R01_0104	5.3	M	PM	A6Va/A6Vb	
#44	R01_0069	6.6	F	PM	A6DR	
#45	R01_0070	6.6	F	PM/dlPFCv	A8aV/A6Va	
#49	R01_0076	8.9	M	dlPFCv	A8aV	o
#63	R01_0091	2.4	M	dlPFCv	A8aV	o
#36	R01_0057	4.1	F	dlPFCv	A8aV	o
#42	R01_0063	8.3	M	dlPFCv	A8aV	o
#46	R01_0075	5.6	F	dlPFCv	A8aV	o
#22	R01_0029	5	F	dlPFCv	A8aV	o
#28	R01_0040	5.6	M	dlPFCv	A8aV	o
#43	R01_0064	8.3	M	dlPFCv/vlPFC	A8aV/A47L	
#77	R01_0110	6.7	F	dlPFCv	A45	o
#23	R01_0030	5.3	F	vlPFC	A47L/A47M	
#29	R01_0043	3.3	F	dlPFCd	A8aD	o
#31	R01_0048	2.4	F	dlPFCd	A8aD	o
#62	R01_0088	3.7	F	dlPFCd	A8aD	o
#19	R01_0026	5	F	dlPFCd	A8aD	o
#21	R01_0028	5.1	M	dlPFCd/FP	A10/A46D	
#30	R01_0046	3.4	M	dlPFCd	A8aD	o
#33	R01_0054	8.1	F	dlPFCd/dmPFC	A8aD/A9/A8b	
#38	R01_0059	8.1	M	dlPFCd	A8aD	o
#41	R01_0062	8.5	M	dlPFCd/dmPFC	A8aD/A9	
#48	R01_0071	7.8	M	dmPFC	A9	o
#60	R01_0094	10.8	M	dmPFC	A9	o
#55	R01_0080	7.4	F	dmPFC	A9/A8b	o
#65	R04_0095	2.6	F	dmPFC	A8b	o
#54	R01_0081	7.6	F	dmPFC	A8b	o
#47	R01_0052	6.2	F	FP	A46V/A10/A47L	o
#58	R04_0080	3.2	F	FP	A10	o
#50	R01_0072	10.4	F	ACC	A32	o
#80	R01_0112	6	F	ACC	A32/A9	
#64	R01_0092	2.4	M	ACC	A24a	o
#69	R01_0095	2.3	M	ACC	A32/A32v/A14R	o
#81	R01_0114	9.8	F	ACC	A25	o
#52	R01_0078	8.9	F	OFC	A13L/A13M	o
#67	R01_0090	2.9	F	OFC	A13M/A13L	o
#78	R01_0107	2.5	M	OFC	A13L	o
#75	R04_0058	5	F	OFC	A11	o
#73	R01_0098	3.3	M	dACC	A24b/A24c	
#82	R01_0115	8.4	F	dACC	A32/A24b	
#83	R04_0023	5.2	M	vlPFC	A47O/A47L	

Table S1.

Marmoset injections analyzed in the present study.

Data ID	injection	experiment_page_url
112458114	ACAd	http://connectivity.brain-map.org/projection/experiment/112458114
139426984	ACAd	http://connectivity.brain-map.org/projection/experiment/139426984
146593590	ACAd	http://connectivity.brain-map.org/projection/experiment/146593590
112514202	ACAv	http://connectivity.brain-map.org/projection/experiment/112514202
139520203	ACAv	http://connectivity.brain-map.org/projection/experiment/139520203
100140756	FRP	http://connectivity.brain-map.org/projection/experiment/100140756
157556400	ILA	http://connectivity.brain-map.org/projection/experiment/157556400
100141454	MOs	http://connectivity.brain-map.org/projection/experiment/100141454
112952510	MOs	http://connectivity.brain-map.org/projection/experiment/112952510
141602484	MOs	http://connectivity.brain-map.org/projection/experiment/141602484
141603190	MOs	http://connectivity.brain-map.org/projection/experiment/141603190
157710335	MOs	http://connectivity.brain-map.org/projection/experiment/157710335
180709942	MOs	http://connectivity.brain-map.org/projection/experiment/180709942
180719293	MOs	http://connectivity.brain-map.org/projection/experiment/180719293
180916954	MOs	http://connectivity.brain-map.org/projection/experiment/180916954
585025284	MOs	http://connectivity.brain-map.org/projection/experiment/585025284
112306316	ORBl	http://connectivity.brain-map.org/projection/experiment/112306316
170721670	ORBl	http://connectivity.brain-map.org/projection/experiment/170721670
180673746	ORBl	http://connectivity.brain-map.org/projection/experiment/180673746
180709230	ORBl	http://connectivity.brain-map.org/projection/experiment/180709230
126860974	ORBm	http://connectivity.brain-map.org/projection/experiment/126860974
112423392	ORBvl	http://connectivity.brain-map.org/projection/experiment/112423392
158435116	ORBvl	http://connectivity.brain-map.org/projection/experiment/158435116
157711748	PL	http://connectivity.brain-map.org/projection/experiment/157711748

Table S2.

Mouse data analyzed in the present study.

Movie S1.

Columnar cortical projections from the marmoset PFC

Three-dimensional presentation of the cortical projections from a PFC injection (A8aD) in the standard reference space. White matter signals are shown in red.

Movie S2.

Contralateral columnar projection in 3D

Three-dimensional reconstitution of the contralateral projections at high resolution.

Movie S1.

Focal and Spread Corticostriatal projections

Three-dimensional reconstitution of the corticostriatal projections. Focal and Spread type projections are visualized in turn for representative samples.

See Brain/MINDS webpage for these movies.

https://dataportal.brainminds.jp/marmoset-tracer-injection/media